

UKAEA-CCFE-PR(21)49

Phillip Gopon, James O. Douglas, Frederick  
Meisenkothen, Jaspreet Singh, Andrew J. London,  
Michael P. Moody

# **Atom probe tomography for isotopic analysis: development of the 34S/32S system in sulfides**

Enquiries about copyright and reproduction should in the first instance be addressed to the UKAEA Publications Officer, Culham Science Centre, Building K1/O/83 Abingdon, Oxfordshire, OX14 3DB, UK. The United Kingdom Atomic Energy Authority is the copyright holder.

The contents of this document and all other UKAEA Preprints, Reports and Conference Papers are available to view online free at [scientific-publications.ukaea.uk/](https://scientific-publications.ukaea.uk/)

# **Atom probe tomography for isotopic analysis: development of the $^{34}\text{S}/^{32}\text{S}$ system in sulfides**

Phillip Gopon, James O. Douglas, Frederick Meisenkothen,  
Jaspreet Singh, Andrew J. London, Michael P. Moody



# MICROSCOPY AND MICROANALYSIS



## Atom probe tomography for isotopic analysis: development of the $^{34}\text{S}/^{32}\text{S}$ system in sulfides

Journal:	<i>Microscopy and Microanalysis</i>
Manuscript ID	Draft
Manuscript Type:	Original Article
Date Submitted by the Author:	n/a
Complete List of Authors:	Gopon, Phillip; University of Leoben, Dept. of Applied Geosciences and Geophysics; University of Oxford, Dept. of Materials; University of Oxford, Dept. of Earth Sciences Douglas, James; University of Oxford, Dept. of Materials Meisenkothen, Frederick; National Institute of Standards and Technology, Materials Measurement Science Division Singh, Jaspreet; University of Oxford, Dept. of Materials London, Andrew; UKAEA; University of Oxford, Dept. of Materials Moody, Michael; University of Oxford, Dept. of Materials
Keywords:	Geology Atom Probe, Nanogeochemistry, Nanoisotopic analysis, S isotopes
Keywords:	Pyrite, Atom Probe Tomography, Sulfides, APT
Abstract:	Using a combination of simulated data and pyrite isotopic reference materials, we have refined a methodology to obtain quantitative $\delta^{34}\text{S}$ measurements from atom probe tomography (APT) datasets. This study builds on previous attempts to characterize relative $^{34}\text{S}/^{32}\text{S}$ ratios in gold containing pyrite using APT. We have also improved our understanding of the artefacts inherent in laser pulsed APT of insulators. Specifically, we find the probability of multi-hit detection events increases during the APT experiment, which can have a detrimental effect on the accuracy of the analysis. We demonstrate the use of

	<p>standardized corrected time-of-flight single-hit data for our isotopic analysis. Additionally, we identify issues with the standard methods of extracting background corrected counts from APT mass spectra. These lead to inaccurate and inconsistent isotopic analyses due to human variability in peak ranging and issues with background correction algorithms. In this study, we use the corrected time-of-flight single-hit data, an adaptive peak fitting algorithm, and an improved deconvolution algorithm to extract <math>^{34}\text{S}/^{32}\text{S}</math> ratios from the <math>\text{S}_2^{++}</math> peaks. By analyzing against a standard material, acquired under similar conditions, we have extracted <math>\delta^{34}\text{S}</math> values to within <math>\pm 5 \text{ ‰}</math> (<math>1 \text{ ‰} = 1 \text{ part per thousand}</math>) of the published values of our standards.</p>

SCHOLARONE™  
Manuscripts

1 **Atom probe tomography for isotopic analysis:**  
2 **development of the  $^{34}\text{S}/^{32}\text{S}$  system in sulfides**  
3

4 Phillip Gopon<sup>1,2</sup>, James O. Douglas<sup>2</sup>, Frederick Meisenkothen<sup>3</sup>, Jaspreet Singh<sup>2</sup>,

5 Andrew J. London<sup>4</sup>, Michael P. Moody<sup>2</sup>

6  
7  
8  
9  
10  
11  
12  
13 *<sup>1</sup>Dept. of Applied Geosciences and Geophysics, University of Leoben, Leoben, AT, 8700*

14 *<sup>2</sup>Dept. of Materials, University of Oxford, Oxford, UK, OX1 3PH*

15 *<sup>3</sup>Materials Measurement Science Division, National Institute of Standards and Technology,*  
16 *Gaithersburg, MD, USA, 20889*

17 *<sup>4</sup>UK Atomic Energy Authority, Culham Science Center, Oxfordshire, UK, OX14 3DB*

**19 Abstract**

20 Using a combination of simulated data and pyrite isotopic reference materials, we have  
21 refined a methodology to obtain quantitative  $\delta^{34}\text{S}$  measurements from atom probe tomography  
22 (APT) datasets. This study builds on previous attempts to characterize relative  $^{34}\text{S}/^{32}\text{S}$  ratios in  
23 gold containing pyrite using APT. We have also improved our understanding of the artefacts  
24 inherent in laser pulsed APT of insulators. Specifically, we find the probability of multi-hit  
25 detection events increases during the APT experiment, which can have a detrimental effect on  
26 the accuracy of the analysis. We demonstrate the use of standardized corrected time-of-flight  
27 single-hit data for our isotopic analysis. Additionally, we identify issues with the standard  
28 methods of extracting background corrected counts from APT mass spectra. These lead to  
29 inaccurate and inconsistent isotopic analyses due to human variability in peak ranging and issues  
30 with background correction algorithms. In this study, we use the corrected time-of-flight single-  
31 hit data, an adaptive peak fitting algorithm, and an improved deconvolution algorithm to extract  
32  $^{34}\text{S}/^{32}\text{S}$  ratios from the  $\text{S}_2^{++}$  peaks. By analyzing against a standard material, acquired under  
33 similar conditions, we have extracted  $\delta^{34}\text{S}$  values to within  $\pm 5 \text{‰}$  ( $1 \text{‰} = 1 \text{ part per thousand}$ ) of  
34 the published values of our standards.

35



## 36           **1. Introduction**

37           Isotopes are important tracers of geologic processes that allow us to track climate change,  
38 determine the ages of minerals, and trace a plethora of geochemical pathways. This paper  
39 presents a range of instrumental and data processing issues, as well as practical workarounds that  
40 allow for the extraction of isotopic data from atom probe data sets of sulfide minerals. Using the  
41 analyses of pyrite reference materials as well as simulated datasets as a baseline, we have  
42 improved our data acquisition protocols to minimize instrumental artefacts and have refined our  
43 data processing algorithms to more accurately and reproducibly extract  $^{34}\text{S}/^{32}\text{S}$  ratios from the  
44  $\text{S}_2^{++}$  family of peaks.

45           The work was initially developed in order to identify the sources of discreet hydrothermal  
46 fluid pulses that are recorded as nanoscale growth zones in gold bearing pyrite (Gopon et al.,  
47 2019). As such, the materials we use are related to this application. However, the methodologies  
48 developed here are relevant to research investigations far beyond this narrow application, as  
49 many of the geochemical processes we aim to track present themselves as similar nanoscale  
50 growth zones in minerals (Haase et al., 1980; Schertl et al., 2012; Valley et al., 2015; Boucher,  
51 2018, etc.). Furthermore, the instrumental and data processing artefacts that we have identified  
52 will be of interest to anyone who uses atom probe tomography (APT), especially in the  
53 measurement of ceramics and other insulating materials (Chen et al., 2009; Thuvander et al.,  
54 2011).

55           The ability to characterize isotopic changes at the nanoscale (and smaller) has the potential to  
56 unlock a new level of detail in these geochemical processes. APT is one of the few techniques  
57 that can obtain spatially correlated isotopic information at the nanoscale. APT has already  
58 transformed our notions of radiogenic elemental mobility in zircon (Valley et al., 2015; Peterman

59 et al., 2016) and been successfully employed in U/Pb dating (Valley et al., 2014; Fougereuse et  
60 al., 2018; Seydoux-Guillaume et al., 2018). However, the application of APT to stable isotopic  
61 systems has had limited application (Daly et al., 2018; Gopon et al., 2020; Meisenkothen et al.,  
62 2020c). This is primarily due to small isotopic shifts in most of these systems and the relatively  
63 large compositional uncertainties often encountered in APT (London, 2019). However, while  
64 other mass spectrometry techniques used for geological applications (e.g., Secondary Ion Mass  
65 Spectrometry [SIMS]) have low useful ion yields (Hervig et al., 2006), APT has a high combined  
66 ionization and detection efficiency of up to 80%. APT, thus, theoretically requires a sampled  
67 volume roughly an order of magnitude smaller than that required by other mass spectrometry  
68 techniques to achieve a given level of analysis precision (Fougereuse et al., 2020). However, the  
69 precision and accuracy of the technique has been hampered by poorly understood instrumental  
70 artefacts, complicated mass spectra, isobaric interferences, and operator-induced errors during  
71 the data processing (Cairney et al., 2015). If all of these issues can be adequately addressed, then  
72 APT genuinely has the potential to unlock new insights into geochemical processes operating at  
73 the nanoscale, at precision levels similar to the micrometer scale techniques currently employed.

74 As most geologic materials are insulators, it is usually necessary to use a laser-pulsing mode  
75 to induce field evaporation, rather than a voltage pulsing mode (Gault et al., 2012). In this mode,  
76 the sample is kept under a localized standing field, and evaporation is instigated through the  
77 pulsing of a laser on the sample apex. Experiments are usually operated at a set ion detection  
78 rate. To maintain this rate, the standing electric field must be continuously increased to keep a  
79 constant evaporation field at the apex of the specimen which gradually blunts over the course of  
80 the experiment. The addition of laser-pulsing capability to a commercial local electrode atom  
81 probe (LEAP) is a relatively recent feature, and has only been available since 2005 (Bunton et

82 al., 2006). As such, the instrument-associated errors induced are less well understood than with  
83 traditional, voltage pulsed, APT. Combine this with the fact that the naturally occurring minerals  
84 geologist study are predominantly ionically and/or covalently bonded (with little to no metallic  
85 character) (Nesse, 2000), have a tendency to evaporate as complex polyatomic molecules rather  
86 than individual ions, and are generally more chemically complex than synthetic materials. All of  
87 these factors have made the generation and interpretation of high precision datasets that much  
88 more difficult. The main challenges for accurate quantification thus lie in correcting the  
89 numerous isobaric interferences inherent in these mass spectra (Figure 1; i.e.  $S_2^{++}$  on  $S^+$ , Ni on Fe  
90  $^{+}/^{++}$ ,  $Cu^{++}$  on  $S^+$ ,  $Zn^{++}$  on  $S^+$ , etc.), understanding and correcting for any instrumental biases, and  
91 removing errors from the data processing steps.

92 This work is focused on a method to correct the isobaric interferences in the mass spectra of  
93 pyrite ( $FeS_2$ ) to obtain accurate  $^{34}S/^{32}S$  ratios, and to shed new light on the instrumental artefacts  
94 of laser pulsed APT. We build on the work of Gopon et al. (2019, 2020) and Meisenkothen et al.  
95 (Meisenkothen et al., 2020a, 2020c) which provided methods for the isotopic analysis of  
96 minerals using APT. By analyzing a set of well-characterized S isotope standards as well as  
97 simulated APT datasets, we have developed a better understanding of the artefacts inherent in  
98 laser pulsed APT. Using what we learned to refine our methodology, we are able to not only  
99 show relative differences in  $^{34}S/^{32}S$  (as in (Gopon et al., 2019)) but can now convert these ratios  
100 into quantitative  $\delta^{34}S$  ratios by running against known reference materials acquired under similar  
101 APT run conditions. This standard-based APT analysis allowed us to accurately determine  $\delta^{34}S$   
102 in pyrite to within  $\sim 5$  ‰ (expressed in parts per thousand difference from a standard; Coplen,  
103 1993). This new capability for APT has wide-ranging applications: including cosmochemistry,  
104 ore geology, bio-geochemistry, and igneous and metamorphic petrology.

## 105           **2. Methods**

106           A set of pyrite isotopic reference materials were provided by Dr. Brian Beard (University of  
107           Wisconsin). These reference materials, called Ruttan and Balmat pyrite, were previously  
108           characterized by Crowe and Vaughan (1996), and have been routinely used as S isotope  
109           reference materials (Hauri et al., 2016; Tanner et al., 2016; Walters et al., 2019). Individual  
110           grains of each of the reference materials were mounted in resin in a standard 25 mm round. The  
111           grains were then polished in a series of successively finer polishing steps using diamond  
112           suspensions, ending with a 1  $\mu\text{m}$  final polish. The samples were then coated with a 20 nm thick  
113           carbon coating, to ensure conductivity in the scanning electron microscope (SEM), and  
114           transferred into a Zeiss Crossbeam 540 dual beam Focused Ion Beam (FIB)-SEM, located in the  
115           David Cockayne Centre for Electron Microscopy at the University of Oxford.

116           A standard FIB-SEM sample preparation protocol was followed (Thompson et al., 2007), in  
117           order to fabricate the highly sharpened needle shaped specimens required for APT. Care was  
118           taken to have the final polished needles maintain, as close as possible, a constant initial tip radius  
119           and shallow shank angle ( $<10^\circ$  shank angle and  $\sim 22$  nm initial tip radius). Samples were run on  
120           the CAMECA LEAP 5000 XR located within the Atom Probe Group of the University of Oxford  
121           Department of Materials. APT experimental conditions were based on previous analyses of  
122           pyrite (Gopon et al., 2019), but purposefully iterated to observe the influence of different run  
123           conditions on the data quality. The instrument was also operated in the “constant charge-state”  
124           mode, where instead of increasing the voltage to maintain a constant detection rate, the voltage  
125           and laser energy are adjusted to maintain a constant ratio in the frequency at which charge-states  
126           for a specific ion are observed (in our case  $\text{S}^+$  at 32 Da and  $\text{S}_2^+$  at 64 Da).

127 For reference we report the  $\text{Fe}^{++}/\text{Fe}^+$  charge state ratio (CSR) as well as the multi-hit  
128 proportion of each of our datasets. Charge state ratios are related to the electric field the sample  
129 experiences during field evaporation and can be an important metric used to reproduce  
130 experimental conditions between different samples (Prosa et al., 2017). A direct relationship  
131 exists between the CSR and electric field strength, and has been computed for  $\text{Fe}^{++}/\text{Fe}^+$  but not  
132  $\text{S}^{++}/\text{S}^+$  (Haycock and Kingham, 1980; Gault et al., 2012). The detected multi-hit percentages  
133 were calculated using \*.ePOS files generated from reconstructions generated in the Integrated  
134 Visualization and Analysis Software (IVAS; v3.8.8), and indicate the percentage of recorded  
135 detector hits that originate from multiple detection events (i.e. when more than one hit is  
136 associated with a given laser pulse event).

137 3-D volume reconstructions of the specimens were undertaken using the IVAS (v3.8.8)  
138 software package, but the majority of compositional and isotopic data analysis was conducted  
139 using a set of purpose-built scripts (see sections 2.1, 2.2). These scripts were primarily used to  
140 accurately and reproducibly determine the peak counts as well as to back calculate the starting  
141  $^{34}\text{S}/^{32}\text{S}$  ratio from the  $\text{S}_2^+$  peak family. The  $\text{S}_2^+$  peak family is used rather than  $\text{S}^+$  due to the  
142 overlap of  $\text{S}_2^{++}$  on  $\text{S}^+$ . The accuracy of these scripts, as well as IVAS, was tested against a series  
143 of simulated APT datasets, and the most accurate method was then applied to the datasets  
144 acquired on the standards. Each of these methods is described in detail below.

### 145 *2.1 Determination of peak counts*

146 APT software requires the operator to manually select the range of mass-to-charge-state ratio  
147 (m/z) values that define the width of each peak in the spectrum (known as ‘ranging’ the data).  
148 The relative shape and width of a given peak might appear to change due to the number of counts  
149 at that peak (i.e. the more counts the wider the peak appears), the operating conditions of the

150 machine (i.e. higher laser pulse energy generally results in wider peaks), and the evolution of the  
151 voltage curve over the course of an APT experiment. Hence, this manual ranging leads to a  
152 source of uncertainty and impacts the reproducibility of the technique (Haley et al., 2015; Blum  
153 et al., 2018; La Fontaine et al., 2018). It should be noted that this uncertainty has a small effect  
154 when calculating the bulk composition of a material. However, since this study is focused on  
155 determining S isotopic ratios to a higher level of accuracy than most APT analyses, it is  
156 necessary to minimize this user artefact.

157 To test and to minimize user induced uncertainty in ranging, various protocols (standard  
158 ranging, constant ranging, Gaussian fit, and adaptive peak fitting) were developed/adapted to  
159 facilitate accurate and repeatable determination of peak counts with minimal user input. Full  
160 descriptions of these methods follow.

### 161 *2.1.1 “Standard” Ranging by eye*

162 The most commonly used method of data reduction is the commercial IVAS software and  
163 ranging “by eye” to determine an appropriate region that corresponds to a specific peak. The  
164 “decomposition” tool in IVAS can then be used to determine the background corrected counts  
165 for the defined range. Alternatively, the MATLAB script package ‘AtomProbeLab’  
166 (<https://sourceforge.net/projects/atomprobelab/>) can be used to extract these counts.

167 To test the precision and reproducibility of this method and the differences between IVAS and  
168 AtomProbeLab, we asked three experienced APT users to range and process simulated APT  
169 datasets as they saw fit. No guidance beyond this was given other than for the user to apply their  
170 “normal” ranging protocol, and the authors were not told how the user “normally” determines  
171 ranges. After the data were processed, the test subjects were asked to describe their ranging  
172 protocol. User 1 used wide ranges that started just left of the peak and ended where the next peak

173 began. User 2 used narrower but near-constant width ranges and iterated the center of the range  
174 after visually inspecting the background determination subjectively for accuracy until the  
175 background was deemed acceptable. User 3 used wide ranges that started just before the peak  
176 and continued until it intercepted the global background or, if the global background was not  
177 reached, until the beginning of the next peak was reached.

178 These ranges were then processed through the IVAS “decomposition” tool as well as  
179 AtomProbeLab to determine the background corrected counts for each peak range. Details of the  
180 background correction algorithms built into IVAS and Atom Probe Lab can be found in (Larson  
181 et al., 1999) and on the AtomProbeLab website (<https://sourceforge.net/projects/atomprobelab/>).  
182 Full details of the ranges used are reported in Appendix A.

### 183 *2.1.2 Constant ranging*

184 In AtomProbeLab, range widths are given by a start (pre-peak width) and end (post-peak  
185 width) which have units of  $\sqrt{\text{Da}}$ . If pre- and post-peak widths are the same, say  $0.01 \sqrt{\text{Da}}$ , and  
186 the peak is at 30 Da, then the m/z range bounds are given by:

$$187 \quad 30 - 0.01 * \sqrt{30} = 29.945 \text{ Da}$$

188 And

$$189 \quad 30 + 0.01 * \sqrt{30} = 30.055 \text{ Da}$$

190 This gives a range scaling which is constant in time-of-flight space, since time of flight is  
191 directly proportional to the square root of m/z. The peak positions are given by the theoretical  
192 isotopic masses from tabulated elemental data.

### 193 *2.1.3 Gaussian fit*

194 The adaptive peak fitting approach assumes all isotopic variants within a single ion species  
195 share the same peak form. The assumption has been supported by empirical observations on  
196 several different materials. Once the assumption is made, the important measurement parameter  
197 is the peak height, not the integrated peak area, since the area will scale in direct proportion to  
198 the peak height. Therefore, alternative peak fitting methods that accurately assesses the relative  
199 peak heights of the isotopic variants could yield analysis results with comparable accuracy. For  
200 the corrected time-of-flight (TOF) spectra encountered in the present work, the peaks of interest  
201 are generally well separated and the upper half of the peaks (Full Width at Half Maximum,  
202 FWHM) can be modeled approximately by a Gaussian function, particularly for the single-hit  
203 spectra. Generally, the continuum contribution under each peak - the combined background and  
204 adjacent overlapping tails - was approximated by a linear model. For the Gaussian peak fitting  
205 script, the analyst chooses a range of corrected TOF values that contains the peak of interest.  
206 Either one or two additional ranges are chosen adjacent to the specified peak range, as  
207 appropriate, for use in the linear regression model and estimation of the continuum contribution  
208 that must be subtracted away from under the peak. After the continuum contribution is removed  
209 from the peak, the script uses a non-linear least squares algorithm to fit a Gaussian function to  
210 the region of the peak spanned at the FWHM. The summit intensity for the peak is then reported  
211 as the output and used in the isotopic analysis.

### 212 *2.1.4 Adaptive peak fitting*

213 Experimental observations have shown the isotopic variants of an ion species - e.g.,  
214  $^{32,32}\text{S}_2^+$ ,  $^{32,33}\text{S}_2^+$ ,  $^{32,34}\text{S}_2^+$ ,  $^{32,36}\text{S}_2^+$ ,  $^{33,33}\text{S}_2^+$ ,  $^{33,34}\text{S}_2^+$ ,  $^{33,36}\text{S}_2^+$ ,  $^{34,34}\text{S}_2^+$ ,  $^{34,36}\text{S}_2^+$ ,  $^{36,36}\text{S}_2^+$  - have  
215 nominally the same peak form (Meisenkothen et al., 2020c, 2020a, 2020b). The local spectrum



216 in the region of the family of peaks can thus be approximated as a linear combination of the  
217 individual constituent peaks, and an optimization algorithm can be used to determine the “best  
218 fit” shape, shared in common by the peaks, and the relative intensities of the peaks. The method  
219 has been described as “adaptive peak fitting,” because the peak form is not assumed *a priori*.  
220 Rather, the algorithm uses an iterative approach to solve for the common peak form, channel by  
221 channel, by minimizing the residual sum of squares as a cost function. We are currently using the  
222 limited-memory Broyden-Fletcher-Goldfarb-Shanno algorithm with box constraints (L-BFGS-B  
223 (Byrd et al., 1995)) to perform the optimization in our analyses. The box constraints are  
224 necessary to ensure all solutions are non-negative and to reduce fitting artifacts. A detailed  
225 outline of an earlier version of the adaptive peak fitting code is provided in Meisenkothen et al.  
226 (2020c). The background spectrum under the family of peaks was assumed to be a constant and  
227 was approximated by averaging the ion counts in hundreds of bins immediately to the left of the  
228 family of peaks. Adaptive peak fitting has been used successfully to provide repeatable and  
229 accurate isotopic analyses with filtered single-hit corrected TOF spectra collected for a variety of  
230 materials on a LEAP-4000XSi instrument (Meisenkothen et al., 2020c, 2020a, 2020b). All of our  
231 analyses performed with the adaptive peak fitting used corrected TOF spectra exported from the  
232 IVAS (v 3.8.8) Cal/Recon Wizard (i.e., timing signal-only-based data, prior to hit finding and ion  
233 feedback filtering) with a bin width of 0.01 ns. Prior work has demonstrated the ion data  
234 recorded in the IVAS Cal/Recon Wizard corrected TOF spectrum can differ significantly from  
235 that recorded in the \*.ePOS file, and the most accurate isotopic analysis results were achieved by  
236 employing a consistent analysis methodology on the single-hit corrected TOF data  
237 (Meisenkothen et al., 2020c, 2020a, 2020b). Similarly, for silicon specimens of natural isotopic  
238 abundance, Prosa and Oltman (2021) have reported their most accurate isotopic analysis results

239 were obtained with non-default RHIT files that had been generated without prompt ion feedback  
240 filtering of multi-hit events and by using consistent automated ranging strategies.

241 The analysis of the  $S_2^+$  peaks is challenging for the current generation adaptive peak  
242 fitting algorithm. The proximity of each peak to its neighbors means the algorithm has little  
243 information upon which to draw as it tries to “learn” what the underlying spectrum should be  
244 beneath each peak. Therefore, box constraints are used to impose upper and lower bounds within  
245 which a solution must be found over a specified range of corrected TOF values. Fortunately, the  
246 empirical  $S_2^+$  peaks we have encountered thus far are generally well separated, so cascading  
247 overlapping peak tails need not be solved by the fitting algorithm and accurate peak forms can be  
248 determined.

249

## 250 2.2 $^{34}S/^{32}S$ deconvolution algorithms

251 Because of the isobaric interference of  $S_2^{++}$  on the four stable  $S^+$  isotope peaks (i.e. 32 Da, 33  
252 Da, 34 Da, 36 Da), as well as the interferences of  $O^+$ ,  $OH^+$ , and  $H_2O^+$  on the  $S^{++}$  peaks, the only  
253 place in the mass spectrum where there is a complete set of sulfur peaks without interference is  
254 at the  $S_2^+$  location (64 Da, 65 Da, 66 Da, 67 Da, 68 Da, 69 Da, 70 Da, 72 Da; Figure 1).

255 However, the multiple combinations of sulfur isotopes ( $^{32}S+^{32}S \rightarrow 64$  Da,  $^{32}S+^{33}S \rightarrow 65$  Da,  
256  $^{33}S+^{33}S \rightarrow 66$  Da,  $^{32}S+^{34}S \rightarrow 66$  Da,  $^{33}S+^{34}S \rightarrow 67$  Da,  $^{32}S+^{36}S \rightarrow 68$  Da,  $^{34}S+^{34}S \rightarrow 68$  Da,  
257  $^{33}S+^{36}S \rightarrow 69$  Da,  $^{34}S+^{36}S \rightarrow 70$  Da, and  $^{36}S+^{36}S \rightarrow 72$  Da) that can comprise the molecules in the  
258  $S_2^+$  family of peaks, makes extracting the  $^{34}S/^{32}S$  ratios difficult. To determine the relative  
259 amounts of  $^{32}S$ ,  $^{33}S$ ,  $^{34}S$ , and  $^{36}S$  that contributed to the observed 64 Da, 65 Da, 66 Da, 67 Da, 68  
260 Da, 69 Da, 70 Da, and 72 Da peaks, three methods were developed and tested (Monte Carlo,

261 Multinomial, and Linear Least Squares). Due to experimental considerations, only the 64 Da, 65  
262 Da, 66 Da, 67 Da, and 68 Da peaks were considered in these calculations.

### 263 *2.2.1 Estimating isotope abundance: Monte Carlo approach*

264 The Monte Carlo approach, which was previously developed for relative  $^{34}\text{S}/^{32}\text{S}$  comparisons  
265 and is described in more detail in Gopon et al. (2019, 2020), was applied here to attempt to  
266 simulate the random combinations of sulfur ions during the analysis and make up the peaks in  
267 our data. This is achieved by populating two data tables with the same proportion of the numbers  
268 32, 33, 34, and 36, with each table representing one of the S atoms in an  $\text{S}_2^+$  ion. These values  
269 are initially in the proportions of a representative natural isotopic abundance of S (De Laeter et  
270 al., 2003); i.e. 94.99 % of the numbers are 32, 0.75 % of the numbers are 33, 4.25 % of the  
271 numbers are 34, and 0.01 % of the numbers are 36. A value is randomly pulled from each table,  
272 then summed, and input into a third table. This is repeated  $10^8$  times, and the values in this third  
273 table approximate what a mass spectrum using this isotopic abundance would be, assuming that  
274 the combination of ions is totally random. We then compare the relative counts for each peak in  
275 this table to the values measured from the actual dataset and obtain a mismatch value for the  
276 simulated and real data.

277 A grid search of isotopic guesses is then conducted, iteratively changing the abundance of  $^{32}\text{S}$ ,  
278  $^{33}\text{S}$ ,  $^{34}\text{S}$ , and  $^{36}\text{S}$  over the range of naturally occurring isotopic abundances (McKeegan and  
279 Leshin, 2001; Meija et al., 2016), and calculating the corresponding values of 64 Da, 65 Da, 66  
280 Da, 67 Da, 68 Da, 69 Da, 70 Da, and 72 Da for each combination of S isotopes. We define the  
281 best-fit combination as the one that minimizes the sum of squared residuals between the  
282 observed values and measured values of only the 64 Da, 65 Da, 66 Da, 67 Da, and 68 Da peaks  
283 (as the 69 Da, 70 Da, and 72 Da peaks are either indistinguishable from the noise in the mass

284 spectra and/or have an overlap from  $\text{Fe}_2\text{S}^{++}$ ). It should be noted that equal weight is given to the  
 285 mismatch value for each peak no matter its size or relative amounts of  $^{34}\text{S}$  and  $^{32}\text{S}$  that it might  
 286 contain– i.e. the model assumes it is equally important to fit the low count peaks and the high  
 287 count peaks.

288 The entire process is repeated a total of ten times, increasing the number of guesses over the  
 289 same search area (decreasing size of each search ‘bin’), and averaged to ensure that the global,  
 290 rather than a local, minimum is output as the best solution. The time required to run the initial  
 291 iteration is on the order of tens of minutes, with each iteration taking exponentially longer and  
 292 the final iteration taking a few hours. The full code, average of ten repetitions, takes roughly 8  
 293 hours of computing (using personal computer with a 2.8GHz processing speed).

#### 294 *2.2.2 Estimating isotope abundance: multinomial distribution solution*

295 To work around the large amounts of processing time required for the Monte Carlo  
 296 approach alternative analytical solutions were developed. The following analytical solution is  
 297 based on a multinomial distribution.

298 The probability,  $P$ , of a certain set of outcomes in a given number of events, using the  
 299 multinomial distribution, is given by the following equation.

$$300 \quad (1) \quad P = \frac{n!}{(n_1!)(n_2!)(n_3!)(n_4!)} p_1^{n_1} p_2^{n_2} p_3^{n_3} p_4^{n_4}$$

301 Here, “ $n$ ” is the total number of events (in our case, two, because we are drawing pairs of atoms),  
 302 “ $n_i$ ” is the number of times outcome “ $i$ ” occurs; “ $p_i$ ” is the probability of outcome “ $i$ ” (in this  
 303 case, “ $p$ ” is the relative isotopic abundance), and “ $i$ ” corresponds to a specific mass number (i.e.,  
 304 32, 33, 34, 36). For example, for an ion having a ( $m/z$ ) of 65 Da ( $^{32,33}\text{S}_2^+$ ), the expression would  
 305 simplify to

$$306 \quad (2) \quad P_{32/33} = \frac{2!}{(1!)(1!)(0!)(0!)} p_1^1 p_2^1 p_3^0 p_4^0 = 2p_1 p_2$$

307 For the mass peaks composed of several different diatomic sulfur ions, such as the peak at 66  
 308 Da ( $^{32,34}\text{S}_2^+$  and  $^{33,33}\text{S}_2^+$ ), equation (1) needs to be evaluated for each constituent type of diatomic  
 309 sulfur ion and the results summed. We then get a set of five simultaneous equations that can be  
 310 solved for the four probabilities,  $p_i$ , where  $I_j$  is the relative empirical intensity observed for each  
 311 peak in the spectrum (i.e. 64 Da, 65 Da, 66 Da, 67 Da, and 68 Da).

$$312 \quad (3) \quad p_{32} = \sqrt{I_{64}}$$

$$313 \quad (4) \quad p_{33} = \frac{I_{65}}{2p_{32}}$$

$$314 \quad (5a) \quad p_{34} = \frac{I_{66} - p_{33}^2}{2p_{32}}$$

$$315 \quad (5b) \quad p_{34} = \frac{I_{67}}{2p_{33}}$$

$$316 \quad (6) \quad p_{36} = \frac{I_{68} - p_{34}^2}{2p_{32}}$$

317 Two different expressions are produced for  $p_{34}$ , the abundance of  $^{34}\text{S}$ , and shown as Equations  
 318 5a and 5b. Ideally, these two expressions would yield identical results for the  $^{34}\text{S}$  abundance.  
 319 However, since we are empirically estimating  $p_{34}$ , the results from these two expressions are  
 320 generally not identical – we will thus generate two different values for  $p_{34}$ . In our analyses, we  
 321 have elected to use Equation 5a for estimating  $p_{34}$ . Equation 5a is more robust, from a counting  
 322 statistics standpoint, and exhibits significantly less variability between data sets.

323 *2.2.3 Estimating isotope abundance: non-linear least squares solution*

324 The  $^{34}\text{S}/^{32}\text{S}$  ratio was also calculated using a non-linear least squares solver (MATLAB). The  
 325 peak intensities of the  $\text{S}_2^+$  peaks were calculated using the three most abundant isotopes of S  
 326 only, with abundances  $A_1$  and  $A_2$  for isotopes  $^{32}\text{S}$  and  $^{33}\text{S}$  respectively; the  $^{34}\text{S}$  isotopic abundance  
 327 expressed as  $1-A_1-A_2$ . The total counts are expressed as  $N$  and this is used to normalize the  
 328 measured peak counts  $\mathbf{r}$ , which is a vector length 5. The function to optimize is given by the  
 329 products of the S isotopes contributing to the different  $\text{S}_2$  peaks.

330 (7) 
$$f(A_1, A_2, N) = \begin{bmatrix} A_1^2 \\ 2.A_1A_2 \\ A_2^2 + 2.A_1(1 - A_1 - A_2) \\ 2.A_2(1 - A_1 - A_2) \\ (1 - A_1 - A_2)^2 \end{bmatrix} - \frac{\mathbf{r}}{N}$$

331 There are three variables to optimize and  $\mathbf{r}$  is a fixed value for any given set of peaks. The  
 332 optimization goal of the function  $f$  is to minimize the sum of the squared residuals of each of the  
 333 items of the resultant vector. Note that MATLAB's 'lsqnonlin' function requires the user-defined  
 334 function to compute a vector-valued function.

335 *2.3 Tests of peak count determinations and  $^{34}\text{S}/^{32}\text{S}$  deconvolution algorithms*

336 To test the accuracy of the methods used for extracting peak counts (section 2.1) as well as  
 337 our  $^{34}\text{S}/^{32}\text{S}$  deconvolution algorithms (section 2.2), a series of simulated APT datasets were  
 338 generated using the MATLAB script of London (London, 2019;  
 339 <https://sourceforge.net/projects/atomprobelab/>). In these simulated spectra, we know *a priori* the  
 340 counts at each of the  $\text{S}_2^{++}$  peaks of interest (hereafter referred to as 'actual' counts), as well as the  
 341  $^{34}\text{S}/^{32}\text{S}$  ratio used to create the dataset (hereafter referred to as 'starting' ratio). We, therefore, use  
 342 the simulated spectra to independently test both the methods for extracting counts and the

343 methods for back calculating the  $^{34}\text{S}/^{32}\text{S}$  ratio. The starting sulfur isotopic abundance used was  
 344 kept constant (0.0447084;  $^{34}\text{S}/^{32}\text{S}$ ) for these simulations with only the algorithm used to simulate  
 345 the peaks being iterated (i.e. with increasing level of complexity). However, it should be noted  
 346 that uncertainty from counting statistics for our simulated datasets (containing 10 million ions  
 347 each), means that the 'real'  $^{34}\text{S}/^{32}\text{S}$  ratio might fluctuate by  $7 \times 10^{-6}$  (based on a 95% CI).

348 A series of simulations incorporating an increasing level of complexity was implemented such  
 349 that: Simulation 1 - Delta peak shape with no background; Simulation 2 - Delta peak shape with  
 350 background (signal to noise = 10); Simulation 3 - Gaussian peak shape with no background  
 351 (Gauss sigma = 0.072 Da); Simulation 4 - Gaussian with background (signal to noise = 10,  
 352 Gauss sigma = 0.072 Da); Simulation 5 - Gaussian with background (signal to noise = 10, Gauss  
 353 sigma = 0.3 Da); Simulation 6 - 'Real' peak shape with no background; Simulation 7 - 'Real'  
 354 peak shape with background (signal to noise 10, standard deviation = 0.14 Da); Simulation 8 -  
 355 'Real' peak shape with background (signal to noise 10, standard deviation 0.3 Da). 'Real' peak  
 356 shape denotes a peak form designed to mimic an empirical peak that may be encountered in an  
 357 APT spectrum. Spectra of these simulations are shown in Appendix B.

#### 358 *2.4 Delta Notation*

359 In general, isotopic data in the geosciences are reported not as absolute isotopic ratios, due to  
 360 instrumental issues, but as relative ratios compared to a measured standard. This ratio is referred  
 361 to as delta notation and in our case is calculated as:

$$362 \quad (8) \quad \delta^{34}\text{S} = 1000 \text{‰} \times \left( \frac{\left( \frac{^{34}\text{S}}{^{32}\text{S}} \right)_{\text{sample}}}{\left( \frac{^{34}\text{S}}{^{32}\text{S}} \right)_{\text{reference}}} - 1 \right)$$

363 The notional zero point for sulfur isotopes is Canyon Diablo troilite (CDT), as it is thought to  
 364 represent the most primitive ratio in our solar system (0.0450045; Jensen and Nakai, 1962), and  
 365 analyses are reported compared to that standard. In practice, however, this standard is rarely used  
 366 and instead a secondary standard which was previously measured against CDT is used as a  
 367 standard and the data is corrected to the CDT scale by the following formula:

$$368 \quad (9) \quad \delta^{34}\text{S CDT} = 1000 \text{‰} \times \left( \frac{\left( \frac{{}^{34}\text{S}}{{}^{32}\text{S}} \right)_{\text{sample}}}{\left( \frac{{}^{34}\text{S}}{{}^{32}\text{S}} \right)_{\text{reference}}} - 1 \right) + \delta^{34}\text{S reference}$$

369 We follow the normal convention with the caveat that we report all simulated data against  
 370 the notional CDT value (0.045005) using Equation 8 and report the real APT data both against  
 371 the notional CDT value and by running the two standards against each other using Equation 9.  
 372 Similar  $\delta^x\text{S}$  expressions can be used to quantify the ratio variations in  $^{33}\text{S}/^{32}\text{S}$  and  $^{36}\text{S}/^{32}\text{S}$ .  
 373 However, our focus is on the  $^{34}\text{S}/^{32}\text{S}$  ratio, since this has significance for fluid source  
 374 fingerprinting in geological applications.

### 375 **3. Results**

376 Part of this study was to observe instrumental artefacts inherent in the technique, as well as  
 377 user induced artefacts that come about during data processing. Table 1 shows the results for four  
 378 of the simulated data sets and compares the various methods used to measure relative peak  
 379 intensities. Figure 2 shows the percent difference between the ‘actual’ and the measured relative  
 380 peak intensities for the same four simulated data sets. Figure 3 provides the corresponding  
 381  $^{34}\text{S}/^{32}\text{S}$  ratios for these simulated datasets. As mentioned earlier (section 2.1, 2.2, 2.3), the four  
 382 simulated datasets represent examples of the easiest (Simulation 1), medium difficulty



383 (Simulation 5), and most challenging analysis situations (Simulation 7 and Simulation 8)  
384 provided by the set of eight simulations. The percent difference in Figure 2 is calculated as:

$$385 \quad (10) \quad \textit{Absolute Value} \left( \frac{[\textit{actual counts}] - [\textit{measured counts}]}{[\textit{actual counts}]} \right) * 100$$

386 The full results of the various data processing methods applied to all eight of the simulations can  
387 be found in Appendix C.

388 Figure 2 shows the large scatter inherent in the different ways of determining peak counts. As  
389 Simulation 1 was a delta function with no noise, all methods were able to accurately reproduce  
390 the ‘actual’ counts (zero line). Once more complexity is incorporated into the simulations the  
391 methods deviated significantly, especially in their ability to accurately reproduce the ‘actual’  
392 counts for both the large (ex. 64 Da) and small (ex. 67 Da) peaks. While most of the methods  
393 reproduce the large (64 Da) peak reasonably well, the percent difference of the actual versus  
394 measured for the smallest peak (67 Da) shows deviations greater than 200 % from the actual  
395 (Table 1). The normal ranging ‘by eye’ approach performed poorly for the Gaussian (Simulation  
396 5) compared to the ‘real’ peaks (signal to noise = 10, st.dev. = 0.14 Da) and is off the scale for  
397 Figure 2. However, the worst performance of the ‘by eye’ approach was on the most realistic  
398 simulation (Simulation 8; signal to noise = 10, st.dev. = 0.3 Da). Strangely, the constant range as  
399 well as the Gaussian fit reproduced the small peak intensities (67 Da and 68 Da) for the ‘real’  
400 peak shapes represented by Simulation 7 and Simulation 8 better than the Gaussian distribution  
401 represented by Simulation 5 (~350 % deviation for Gaussian fit of the 67 Da peak). The  
402 Gaussian fit and adaptive peak fitting produced similar levels of accuracy for the ‘real’ peak  
403 shapes (Simulation 7 and Simulation 8), but the most overall consistent method is the adaptive  
404 peak fitting approach.

405 Figure 3 shows the three different approaches for the back calculation of the original  $^{34}\text{S}/^{32}\text{S}$   
406 ratio. The Monte Carlo approach was able to get within ~8 ‰ of the correct answer for  
407 Simulation 1 but failed to get within 20 ‰ of the correct answer for all other simulations (except  
408 when the ‘actual’ counts were used; Figure 3/Table 1). The multinomial and the linear least  
409 squares approach produced the same results for all methods of peak count determination to  
410 within 0.1 ‰ (Table 1) but did deviate from the ‘starting’ ratio possibly due to the counting  
411 statistics inherent in the simulations.

412 Table 2 shows the calculated  $^{34}\text{S}/^{32}\text{S}$  ratios of our empirical datasets from the two pyrite  
413 reference materials (Ruttan and Balmat). All  $^{34}\text{S}/^{32}\text{S}$  ratios are calculated using adaptive peak  
414 fitting (section 2.1.4) to obtain the relative peak intensities and the multinomial approach to  
415 back-calculate the  $^{34}\text{S}/^{32}\text{S}$  ratios (section 2.2.2). Appendix D additionally shows the same data  
416 processed by Gaussian fitting and fitting from IVAS. We also report the corresponding  $\delta^{34}\text{S}$   
417 values, which are calculated against the opposite standard acquired under the same APT run  
418 conditions (see discussion), i.e.  $[^{34}\text{S}/^{32}\text{S}.\text{Balmat}@40\text{pJ}] / [^{34}\text{S}/^{32}\text{S}.\text{Ruttan}@40\text{pJ}]$ . Where two of  
419 the same standards were acquired under the same run conditions, the standard with the closest  
420 dataset number is used (as it is closest in time). Data for the pyrite reference materials were  
421 analyzed over a range of laser energies to ascertain the influence on  $^{34}\text{S}/^{32}\text{S}$ . The standard data of  
422 the two largest datasets (R5083\_0893 and R5083\_0892) are further subdivided over specific  
423 ranges of standing voltage (i.e. time intervals of the analysis) to attempt to isolate the influence  
424 that changes during the progression of the run have on the resultant mass spectra and multi-hit  
425 fraction. Figure 4 shows the results of the progression of the APT experiment (for dataset  
426 R5083\_0893) on the multi-hit fraction. This increase in the multi-hit fraction correlates with a  
427 decrease in the  $\text{Fe}^{++}/\text{Fe}^{+}$  (Figure 5) and was noted to influence the resultant  $^{34}\text{S}/^{32}\text{S}$  ratios (Table

2; Figure 6). The influence of the changing standing field (i.e. progression of the run) is most pronounced on the  $\delta^{34}\text{S}$  calculated against the nominal Canyon Diablo Troilite  $^{34}\text{S}/^{32}\text{S}$  ratio (Equation 8; Figure 6). When the data is compared to a standard acquired using the same analysis conditions (Equation 9) and over the same voltage range the issue becomes less pronounced (Figure 6). When the single hit data over the entire voltage range is used, the best results are obtained and the  $\delta^{34}\text{S}$  was reproduced to within  $\sim 5\%$   $\delta^{34}\text{S}$  of the published values (Crowe and Vaughan, 1996). However, the small number of datasets might mean that this deviation could be larger (for the single-hit or multi-hit data). Note that the ‘entire’ voltage range is never used, but rather we mean during stable data acquisition (i.e. after the initial calibration and before tip failure).

#### 4. Discussion

The careful analysis of reference materials in this study has given us insight into the challenges of laser pulsed APT, as well as highlighting potential solutions to produce quality data. As shown in Figure 6, when the necessary steps are taken to correct analytical issues, our technique reproduced the published  $\delta^{34}\text{S}$  values to within  $\sim 5\%$   $\delta^{34}\text{S}$ .

Rigorous testing of the various methods to determine relative peak intensities and analytical solutions for the back-calculation of  $^{34}\text{S}/^{32}\text{S}$  ratios (Figure 2 and Figure 3) shows that error can be introduced depending on the method of measuring peak intensities. The ‘standard’ ranging approach is the most inconsistent and inaccurate. This is in part due to the inability of the human observer to be able to visualize parts of the peak that are close to the noise threshold. This was most evident with the approach of User 3, who attempted to use ranges that ended when the peak reached the global background (unless another peak was reached first). This led to widely different range widths that by eye still looked appropriate. However, it must be noted that the

451 simulations modeled the same peak width regardless of relative peak height (of which the  
452 analysts were unaware), so the most appropriate ranging should in fact be one that is at least  
453 consistent in its width. Users 1 and 2 did use relatively constant range widths, however the very  
454 wide ranges of User 1 meant that more emphasis was placed on the background correction. Table  
455 1 shows that this over-reliance on the accuracy of the background correction schemes for the  
456 wide ranges used by User 1 and 3, produces data that can be hugely inaccurate (including zero  
457 and negative peak counts; Table 1). Part of the study was to compare different methods of  
458 background correction (i.e. those built into IVAS and AP Lab; Larson et al., 1999; London,  
459 2019) and we note large discrepancies between the methods, even when exactly the same ranges  
460 are used.

461 The lower level of accuracy observed in the peak intensity determination by ‘standard’  
462 ranging has a significant impact on the calculated  $^{34}\text{S}/^{32}\text{S}$ , as evidenced by Table 1. Deviations of  
463  $> 40 \text{ ‰ } \delta^{34}\text{S}$  were noted in the analytical solutions (multinomial and linear least squares; sections  
464 2.2.2/2.2.3) for the simulated data. It must be noted that the Monte Carlo (section 2.2.1) approach  
465 showed large discrepancies in the  $\delta^{34}\text{S}$  values, when compared to the analytical solutions. This is  
466 most likely due to the inability of our Monte Carlo approach to place relative importance on the  
467 individual peaks, as the approach comes up with a best fit for all of the peaks, regardless of the  
468 magnitude of the contribution an individual peak makes to the  $^{34}\text{S}/^{32}\text{S}$  ratio (i.e. it places equal  
469 emphasis on the misfit parameter even if the peak contains no  $^{34}\text{S}$  or  $^{32}\text{S}$ ). The consequence of  
470 this is that when the method used to measure relative peak intensities is inaccurate, it has a  
471 significant detrimental effect on the Monte Carlo solution. This is most pronounced for the 67 Da  
472 peak which all of the methods had the most issue correctly determining the associated peak  
473 counts (Figure 2). The absence of the 67 Da peak from the analytical solution for the  $^{34}\text{S}$

474 abundance found by the multinomial approach and the weighted importance of the larger peaks  
475 for the linear least squares approach, means these two methods do not suffer from the same issue.  
476 Furthermore, the multinomial and linear least squares approaches, relative to the Monte Carlo  
477 method, are less sensitive to any issues related to the determination of relative peak intensities  
478 within the  $S_2^{++}$  family of peaks. The linear least squares and multinomial solutions produce  
479 roughly the same results (to within 0.1 %  $\delta^{34}S$ ), and the preference to use the multinomial  
480 approach for the remaining data processing is simply because the workflow from the adaptive  
481 peak fitting to multinomial is simpler (i.e. the output from one is directly readable by the other).

482 The influence of instrumental artefacts has been investigated with the detrimental influence of  
483 the signal loss to multi-hits being the primary hindrance to obtaining accurate and precise  
484 isotopic data. Figure 4 shows that there is an increase in the relative number of multi-hits as the  
485 experiment progresses (i.e. as the voltage increases). The progression of the APT experiment has  
486 the first order effect of blunting the apex of the sample through field evaporation. This blunting  
487 means the laser is exciting a larger surface area, increasing the probability of an ion evaporation  
488 event. So, while the standing voltage must be increased to compensate for this blunting effect,  
489 the local electric field required for field ionization is actually decreasing (Table 2). This decrease  
490 in local electric field as the APT experiment progresses changes the preferential charge state for  
491 the evaporating ionic species and has the effect of increasing the multi-hit percentage (Figure 5).

492 Based solely on counting statistics, it would seem the more counts present in the molecular  
493  $S_2^+$  peaks we are using to determine the  $^{34}S/^{32}S$  ratio, the greater the precision, and possibly the  
494 accuracy, should be. However, the opposite trend is apparent in our data (Table 2); though, our  
495 assessment may be hampered by the limited number of data sets in our analysis. One possible  
496 explanation for this observed trend is the increased number of multi-hit detection events. Multi-

497 hit detection events can suffer from ion signal loss, as a result of detector dead time effects,  
498 which tends to produce significant isotopic and chemical measurement bias (Saxey, 2011;  
499 Thuvander et al., 2011, 2019; Meisenkothen et al., 2015). If dead-time is a significant factor in  
500 introducing bias into our sulfur isotopic measurements, then we would expect the “All Hit” data  
501 reported in Table 2 to reflect an undercounting of the major isotope ( $^{32}\text{S}$ ), and thus a relative over  
502 counting of the minor isotope ( $^{34}\text{S}$ ). Therefore,  $^{34}\text{S}/^{32}\text{S}$  is expected to be higher for data sets with  
503 more multi-hit detection events. In fact, this is roughly what we observe in Table 2. The 3500 V  
504 to 4500 V range for dataset 8493 has more multi-hits than the 2500 V to 3500 V range, and it has  
505 a higher  $^{34}\text{S}/^{32}\text{S}$ . Likewise, the 8462 and 8460 data sets have a higher multi-hit fraction and a  
506 higher  $^{34}\text{S}/^{32}\text{S}$ , on average, than the 8493 and 11434 data sets. So, while not definitive, these  
507 results are consistent with multi-hit data having an impact on our analysis results. Also, the  
508 average number of multi-hit detection events in data set 9023 ( $^{34}\text{S}/^{32}\text{S} = 0.0458$ ) is similar to that  
509 for data sets 8462 and 8460 (average  $^{34}\text{S}/^{32}\text{S} = 0.0457$ ), so we would expect the  $^{34}\text{S}/^{32}\text{S}$  to be  
510 comparable for these three data sets, which it is. However, in calculating the  $\delta^{34}\text{S}$  value, we take  
511 a ratio of opposite standards  $^{34}\text{S}/^{32}\text{S}$ . Since the opposite standards were collected under similar  
512 acquisition conditions, the multi-hit bias is expected to partially cancel out, since the numerator  
513 and denominator would be similarly affected by the deadtime effects.

514 A potential alternative solution to avoid changes in preferential charge state ratio evaporation  
515 was considered by using our atom probe in the “constant charge state” mode. The hope was that  
516 by maintaining a constant charge state ratio the multi-hit fraction could at least be kept constant  
517 during the run and could then be more easily corrected for. However, this data acquisition mode  
518 produced some of the largest deviations from the nominal  $\delta^{34}\text{S}$ , possibly because changes in laser  
519 energy have a more significant effect on data quality than the voltage evolution.

520 As discussed in section 2.4, isotopic data in the geosciences are often reported relative to a  
521 measured standard. However, this comparison of ratios between standards and unknown is  
522 difficult in APT, as the primary focusing optic in APT is the sample itself. The diameter of the  
523 hemispherical cap and the shank angle of the needle shaped specimen are primarily responsible  
524 for the applied electric field (and thus standing voltage) required to field evaporate ions from the  
525 sample, and the trajectories that the ions take to the detector. For these reasons, standards based  
526 APT has generally been thought of as being impractical, as the artefacts induced by different tip  
527 geometries and shapes were thought to be larger than the instrumental artefacts.

528 However, our work shows the opposite is true, i.e. that the instrumental induced artefacts are  
529 relatively consistent and considerably larger than those seemingly induced by tip geometries, at  
530 least in our sample set where care was taken to produce roughly the same tip geometries (Figure  
531 6/Table 2). Samples must therefore be analyzed against a standard, measured under similar APT  
532 experimental conditions, and ideally sharpened to a similar tip radius and shank angle as the  
533 unknown sample. Confirmation of the lesser influence of the tip geometries is evidenced by the  
534 repeat analysis of the same standards from different APT needles (Table 2), which show between  
535 tip deviations that are smaller than the absolute deviation from the notional isotopic value for our  
536 standards (Figure 6).

537 The increasing standing field has a large effect on the accuracy of our data (Table 2), in a  
538 large part, due to the increased likelihood of multi-hits at higher voltages (Figure 4). The analyst  
539 must be careful to use data from a standard that is comparable in voltage range and/or data  
540 quality regarding multi-hits. Work is ongoing to better understand and to correct this influence.  
541 Several strategies are under consideration, including the use of new detector technology (Kelly,  
542 2020), new laser technology (Chiaramonti et al., 2019), and artificially reducing the detection

543 efficiency to reduce the number of multi-hits (Thuvander et al., 2019). However, the solution  
544 presented herein is to only use filtered single-hit data which is processed using adaptive peak  
545 fitting from Meisenkothen et al., (2020c). Combining this methodology with a reference material  
546 standard acquired under similar conditions (e.g. 80 pJ), produced quantitative results on our  
547 reference materials within  $\pm 5 \text{ ‰ } \delta^{34}\text{S}$  of their published reference values (Crowe and Vaughan,  
548 1996). Considering the difficulty in mathematically assessing the compound influence of  
549 counting statistics, instrumental artefacts, and error in our deconvolution solver; we take the  
550 measured deviation from the nominal standard ratio ( $5 \text{ ‰ } \delta^{34}\text{S}$ ) using our recommended  
551 methodology (standards based APT at 80 pJ of a sample with  $<10^\circ$  shank angle and  $\sim 25\text{nm}$  tip  
552 radius, single-hit corrected TOF spectrum processed with adaptive peak fitting, and multinomial  
553  $34/32$  calculation) as a preliminary estimate of the total error of our technique.

554 We should point out that our technique has currently only been tested in relatively pure pyrite  
555 (i.e. little or no trace elements) and we caution the application to other sulfide minerals before  
556 more thorough testing can be done. The purer the sample is, the less potential for unforeseen  
557 isobaric interferences on the peaks used in our technique. A separate protocol was developed to  
558 correct for small isobaric interferences of Cu on this family of peaks (Gopon et al., 2019) and  
559 would likely need to be expanded upon for more complex sulfides.

560

## 561 **5. Conclusion**

562 This study rigorously analyzed simulated and empirical APT data from pyrite reference  
563 materials in order to develop a method for determining quantitative S isotopic ratios from APT  
564 datasets. We have also obtained a more in-depth understanding of some of the instrumental



565 artifacts (e.g. signal loss due to multi-hits) and data reduction artefacts (produced by inaccurate  
566 and inconsistent ranging and background corrections) inherent in laser pulsed APT and have  
567 identified issues with the ‘standard’ methods of APT data reduction built into IVAS and Atom  
568 Probe Lab. Using the adaptive peak fitting algorithm from Meisenkothen et al. (2020c), we can  
569 accurately and reproducibly extract relative peak intensities which can be converted into  $\delta^{34}\text{S}$   
570 values using the analytical solutions described in section 2.2. We believe this paper shows some  
571 of the major problems and barriers to stable isotopic analysis with APT and how to overcome  
572 many of them. We presented a method whereby we have obtained quantitative  $\delta^{34}\text{S}$  values from  
573 APT data of pyrite to 5 ‰ accuracy.

574 In summary:

- 575 • In order to obtain more precise APT data we need to remove human error in ranging.  
576 We have used an adaptive peak fitting algorithm (Meisenkothen et al., 2020c) to  
577 reproducibly and accurately obtain the counts at each peak without the need to  
578 determine a peak range.
- 579 • A large issue in obtaining accurate  $^{34}\text{S}/^{32}\text{S}$  data from the APT appears to be due to  
580 changes in analysis conditions during an analysis. The increase in voltage appears to  
581 cause more multi-hits, which preferentially removes counts of the highest intensity  
582 peaks and contributes bias to our APT data.
- 583 • Accurate determinations of  $\delta^{34}\text{S}$  values in pyrite appear to only be possible using  
584 known reference materials run as standards under similar acquisition conditions as that  
585 used for the unknown.
- 586 • Using the approach of standards-based atom probe tomography, run under the same  
587 conditions (80 pJ), on samples prepared to similar geometries, and processed in the

588 same way (adaptive peak fitting of the corrected TOF spectra and multi-nominal  
589  $^{34}\text{S}/^{32}\text{S}$  calculation) we were able to obtain the published values of the Ruttan and  
590 Balmat pyrite sulfur isotopic standards to within  $\pm 5 \text{‰}$   $\delta^{34}\text{S}$ .

### 591 *Acknowledgements*

592 The authors would like to acknowledge funding from the following sources. We acknowledge  
593 use of characterization facilities within the David Cockayne Centre for Electron Microscopy,  
594 Department of Materials, University of Oxford, alongside financial support provided by the  
595 Henry Royce Institute [EP/R010145/1]. The Zeiss Crossbeam FIB/SEM used in this work was  
596 supported by EPSRC through the Strategic Equipment Fund Grant: EP/N010868/1. AJL was  
597 supported by the EPSRC Grant [EP/T012250/1]. The LEAP 5000XR used in this study was  
598 funded by an EPSRC Grant [EP/M022803/1].

### 599 *†Disclaimer*

600 Certain commercial equipment, instruments, or materials are identified in this paper in order to  
601 specify the experimental procedure adequately. Such identification is not intended to imply  
602 recommendation or endorsement by the University of Leoben, University of Oxford, National  
603 Institute of Standards and Technology, or UK Atomic Energy Authority, nor is it intended to imply  
604 that the materials or equipment identified are necessarily the best available for the purpose.

605

606

607 **References:**

- 608 Blum, T.B., Reinhard, D.A., Chen, Y., Prosa, T.J., Larson, D.J., and Valley, J.W., 2018,  
609 Uncertainty and Sensitivity Analysis for Spatial and Spectral Processing of Pb Isotopes in  
610 Zircon by Atom Probe Tomography, *in* *Microstructural Geochronology: Planetary Records*  
611 *Down to Atom Scale*, p. 327–350.
- 612 Bunton, J., Lenz, D., Olson, J., Thompson, K., Ulfig, R., Larson, D., and Kelly, T., 2006,  
613 Instrumentation Developments in Atom Probe Tomography: Applications in Semiconductor  
614 Research: *Microscopy and Microanalysis*, v. 12, p. 1730–1731.
- 615 Byrd, R.H., Lu, P., Nocedal, J., and Zhu, C., 1995, A limited memory algorithm for bound  
616 constrained optimization: *SIAM Journal on Scientific Computing*, v. 16, p. 1190–1208.
- 617 Cairney, J.M., Rajan, K., Haley, D., Gault, B., Bagot, P.A.J., Choi, P.P., Felfer, P.J., Ringer,  
618 S.P., Marceau, R.K.W., and Moody, M.P., 2015, Mining information from atom probe data:  
619 *Ultramicroscopy*, v. 159, p. 324–337, doi:10.1016/j.ultramic.2015.05.006.
- 620 Chen, Y.M., Ohkubo, T., Kodzuka, M., Morita, K., and Hono, K., 2009, Laser-assisted atom  
621 probe analysis of zirconia/spinel nanocomposite ceramics: *Scripta Materialia*, v. 61, p. 693–  
622 696, doi:10.1016/j.scriptamat.2009.05.043.
- 623 Chiamonti, A.N., Miaja-Avila, L., Blanchard, P.T., Diercks, D.R., Gorman, B.P., and Sanford,  
624 N.A., 2019, A Three-Dimensional Atom Probe Microscope Incorporating a Wavelength-  
625 Tuneable Femtosecond-Pulsed Coherent Extreme Ultraviolet Light Source: *MRS Advances*,  
626 v. 4, p. 2367–2375, doi:10.1557/adv.2019.296.
- 627 Coplen, T.B., 1993, Reporting of stable carbon, hydrogen, and oxygen isotopic abundances, *in*

- 628 Proceedings of the fifth IAEA Meeting on Stable Isotope Standards and Intercomparison  
629 Materials, p. 31–34.
- 630 Crowe, D.E., and Vaughan, R.G., 1996, Characterization and use of isotopically homogeneous  
631 standards for in situ laser microprobe analysis of  $^{34}\text{S}/^{32}\text{S}$  ratios: *American Mineralogist*,  
632 v. 81, p. 187–193, doi:10.2138/am-1996-1-223.
- 633 Daly, L. et al., 2018, Defining the Potential of Nanoscale Re-Os Isotope Systematics Using  
634 Atom Probe Microscopy: *Geostandards and Geoanalytical Research*, v. 42, p. 279–299,  
635 doi:10.1111/ggr.12216.
- 636 La Fontaine, A. et al., 2018, Atom probe tomography analysis of the reference zircon gj-1: An  
637 interlaboratory study: *Chemical Geology*, v. 495, p. 27–35,  
638 doi:10.1016/j.chemgeo.2018.07.031.
- 639 Fougereuse, D., Kirkland, C., Saxey, D., Seydoux-, A.-M., Guillaume, Rowles, M.R., Rickard,  
640 W.D.A., and Reddy, S.M., 2020, Nanoscale isotopic dating of monazite: *Geostandards and*  
641 *Geoanalytical Research*, v. 44, p. 637–652, doi:10.1111/ggr.12340.
- 642 Fougereuse, D., Reddy, S.M., Kirkland, C.L., Saxey, D.W., Rickard, W.D., and Hough, R.M.,  
643 2018, Time-resolved , defect-hosted , trace element mobility in deformed Witwatersrand  
644 pyrite *Geoscience Frontiers* Time-resolved , defect-hosted , trace element mobility in  
645 deformed Witwatersrand pyrite: *Geoscience Frontiers*, v. 10, p. 55–63,  
646 doi:10.1016/j.gsf.2018.03.010.
- 647 Gault, B., Moody, M.P., Cairney, J.M., and Ringer, S.P., 2012, *Atom Probe Microscopy (Z. M.*  
648 *Hull, R., Jagadish, C., Osgood, R.M. Jr., Parisi, J., Wang, Ed.): New York*, v. 1, 411 p.,  
649 doi:10.1017/CBO9781107415324.004.

- 650 George, F.R., Gaidies, F., and Boucher, B., 2018, Population - wide garnet growth zoning  
651 revealed by LA - ICP - MS mapping : implications for trace element equilibration and syn -  
652 kinematic deformation during crystallisation: *Contributions to Mineralogy and Petrology*, v.  
653 173, p. 1–22, doi:10.1007/s00410-018-1503-0.
- 654 Gopon, P., Douglas, J.O., Auger, M.A., Hansen, L., Wade, J., Cline, J.S., Robb, L.J., and  
655 Moody, M.P., 2019, A nanoscale investigation of Carlin-type gold deposits: An atom-scale  
656 elemental and isotopic perspective: *Economic Geology*, v. 114, p. 1123–1133,  
657 doi:10.5382/econgeo.4676.
- 658 Gopon, P., Singh, J., London, A., Hansen, L., Wade, J., and Moody, M., 2020, Extraction of S  
659 Isotopes from Geologic datasets, *in* Proceedings of the Field Emission Society special APT  
660 software meeting, p. 1, [https://youtu.be/Cqi8\\_aurYrw](https://youtu.be/Cqi8_aurYrw).
- 661 Haase, C.S., Chadman, J., Feinn, D., and Ortoleva, P., 1980, Oscillatory Zoning in Plagioclase  
662 Feldspar: *Science*, v. 209, p. 272 LP – 274, doi:10.1126/science.209.4453.272.
- 663 Haley, D., Choi, P., and Raabe, D., 2015, Guided mass spectrum labelling in atom probe  
664 tomography.: *Ultramicroscopy*, v. 159 Pt 2, p. 338–45, doi:10.1016/j.ultramic.2015.03.005.
- 665 Hauri, E.H., Papineau, D., Wang, J., and Hillion, F., 2016, High-precision analysis of multiple  
666 sulfur isotopes using NanoSIMS: *Chemical Geology*, v. 420, p. 148–161,  
667 doi:10.1016/j.chemgeo.2015.11.013.
- 668 Haycock, R., and Kingham, D.R., 1980, Post-ionization of Field-Evaporated Ions: *Physics*  
669 *Review Letters*, v. 44, p. 1520–1523.
- 670 Hervig, R.L., Mazdab, F.K., Williams, P., Guan, Y., Huss, G.R., and Leshin, L.A., 2006, Useful

- 671 ion yields for Cameca IMS 3f and 6f SIMS: Limits on quantitative analysis: *Chemical*  
672 *Geology*, v. 227, p. 83–99, doi:10.1016/j.chemgeo.2005.09.008.
- 673 Jensen, M.L., Nakai, N., 1962, Sulfur isotope meteorite standards results and recommendations,  
674 *in Biochemistry of Sulfur Isotopes*, NSF Symposium, p. 30–35.
- 675 Kelly, T.F., 2020, Project Tomo: in pursuit of Atomic-Scale Analytical Tomography, *in*  
676 *Proceedings of the Atom Probe Tomography and Microscopy Conference*, p. 1.
- 677 De Laeter, J.R., Böhlke, J.K., De Bièvre, P., Hidaka, H., Peiser, H.S., Rosman, K.J.R., and  
678 Taylor, P.D.P., 2003, Atomic weights of the elements: Review 2000 (IUPAC Technical  
679 Report): *Pure and Applied Chemistry*, v. 75, p. 683–800, doi:10.1351/pac200375060683.
- 680 Larson, D.J., Prosa, T.J., Ulfing, R.M., Geiser, B.P., and Kelly, T.F., 1999, Local Electrode Atom  
681 Probe Tomography: a user's guide: New York, Springer, 328 p., doi:10.1007/978-1-4614-  
682 8721-0.
- 683 London, A.J., 2019, Quantifying Uncertainty from Mass-Peak Overlaps in Atom Probe  
684 Microscopy: *Microscopy and Microanalysis*, v. early onli, p. 1–11,  
685 doi:10.1017/S1431927618016276.
- 686 McKeegan, K.D., and Leshin, L.A., 2001, Chapter 4. Stable Isotope Variations in  
687 Extraterrestrial Materials, *in* Valley, J.W. and Cole, D.R. eds., *Reviews in Mineralogy and*  
688 *Geochemistry*, Vol. 43, *Stable Isotope Geochemistry*, p. 279–318.
- 689 Meija, J. et al., 2016, Isotopic compositions of the elements 2013 (IUPAC Technical Report):  
690 *Pure and Applied Chemistry*, v. 88, p. 293–306, doi:10.1515/pac-2015-0503.
- 691 Meisenkothen, F., Mclean, M., Kalish, I., Samarov, D. V., and Steel, E.B., 2020a, Atom Probe

- 692 Mass Spectrometry of Uranium Isotopic Reference Materials: Analytical Chemistry, v. 92,  
693 p. 11388–11395, doi:10.1021/acs.analchem.0c02273.
- 694 Meisenkothen, F., McLean, M., Kalish, I., Samarov, D., and Steel, E., 2020b, Towards Accurate  
695 and Reproducible Uranium Isotopic Analysis via Atom Probe Mass Spectrometry:  
696 Microscopy and Microanalysis, v. 26, p. 176–177, doi:10.1017/s1431927620013689.
- 697 Meisenkothen, F., Samarov, D. V., Kalish, I., and Steel, E.B., 2020c, Exploring the accuracy of  
698 isotopic analyses in atom probe mass spectrometry: Ultramicroscopy, v. 216, p. 113018,  
699 doi:10.1016/j.ultramic.2020.113018.
- 700 Meisenkothen, F., Steel, E.B., Prosa, T.J., Henry, K.T., and Prakash Kolli, R., 2015, Effects of  
701 detector dead-time on quantitative analyses involving boron and multi-hit detection events  
702 in atom probe tomography: Ultramicroscopy, v. 159, p. 101–111,  
703 doi:10.1016/j.ultramic.2015.07.009.
- 704 Nesse, W., 2000, Introduction to Mineralogy: New York, Oxford University Press, 442 p.
- 705 Peterman, E.M., Reddy, S.M., Saxey, D.W., Snoeyenbos, D.R., Rickard, W.D.A., Fougereuse,  
706 D., and Kylander-clark, A.R.C., 2016, Nanogeochronology of discordant zircon measured  
707 by atom probe microscopy of Pb-enriched dislocation loops: Science Advances, v. 2, p. 1–9,  
708 doi:10.1126/sciadv.1601318.
- 709 Prosa, T.J., and Oltman, E., 2021, Study of LEAP 5000 Deadtime and Precision via Silicon Pre-  
710 Sharpened-Microtip Standard Specimens, *in* Microscopy and Microanalysis, p. 1.
- 711 Prosa, T.J., Reinhard, D.A., Saint-Cyr, H.F., Martin, I., Rice, K.P., Yimeng, C., and Larson, D.J.,  
712 2017, Evolution of Atom Probe Data Collection Toward Optimized and Fully Automated

- 713 Acquisition: *Microscopy and Microanalysis*, v. 23(S1), p. 616–617.
- 714 Saxey, D.W., 2011, Correlated ion analysis and the interpretation of atom probe mass spectra:  
715 *Ultramicroscopy*, v. 111, p. 473–479, doi:10.1016/j.ultramic.2010.11.021.
- 716 Schertl, H.-P., Maresch, W. V., Stanek, K.P., Hertwig, A., Krebs, M., Baese, R., and Sergeev,  
717 S.S., 2012, New occurrences of jadeitite, jadeite quartzite and jadeite-lawsonite quartzite in  
718 the Dominican Republic, Hispaniola: petrological and geochronological overview:  
719 *European Journal of Mineralogy*, v. 24, p. 199–216, doi:10.1127/0935-1221/2012/0024-  
720 2201.
- 721 Seydoux-Guillaume, A.-M., Fougereuse, D., Laurent, A.-T., Gardés, E., Reddy, S.M., and  
722 Saxey, D.W., 2018, Nanoscale resetting of the Th/Pb system in an isotopically-closed  
723 monazite grain: a combined atom probe and transmission electron microscopy study:  
724 *Geoscience Frontiers*, doi:10.1016/j.gsf.2018.09.004.
- 725 Tanner, D., Henley, R.W., Mavrogenes, J.A., and Holden, P., 2016, Sulfur isotope and trace  
726 element systematics of zoned pyrite crystals from the El Indio Au–Cu–Ag deposit, Chile:  
727 *Contributions to Mineralogy and Petrology*, v. 171, p. 1–17, doi:10.1007/s00410-016-1248-  
728 6.
- 729 Thompson, K., Lawrence, D., Larson, D.J., Olson, J.D., Kelly, T.F., and Gorman, B., 2007, In  
730 situ site-specific specimen preparation for atom probe tomography: *Ultramicroscopy*, v.  
731 107, p. 131–139, doi:10.1016/j.ultramic.2006.06.008.
- 732 Thuvander, M., J. Weidow, J., Angseryd, J., Falk, L.K.L., Liu, F., Sonestedt, M., Stiller, K., and  
733 Andr??n, H.O., 2011, Quantitative atom probe analysis of carbides: *Ultramicroscopy*, v.  
734 111, p. 604–608, doi:10.1016/j.ultramic.2010.12.024.



- 735 Thuvander, M., Shinde, D., Rehan, A., Ejnermark, S., and Stiller, K., 2019, Improving  
736 Compositional Accuracy in APT Analysis of Carbides Using a Decreased Detection  
737 Efficiency: *Microscopy and Microanalysis*, v. 25, p. 454–461,  
738 doi:10.1017/S1431927619000424.
- 739 Valley, J.W. et al., 2014, Hadean age for a post-magma-ocean zircon confirmed by atom-probe  
740 tomography: *Nature Geoscience*, v. 7, p. 219–223, doi:10.1038/ngeo2075.
- 741 Valley, J.W., Reinhard, D.A., Cavosie, A.J., Ushikubo, T., Lawrence, D.F., Larson, D.J., Kelly,  
742 T.F., Snoeyenbos, D.R., and Strickland, A., 2015, Presidential Address. Nano- and micro-  
743 geochronology in Hadean and Archean zircons by atom-probe tomography and SIMS: New  
744 tools for old minerals: *American Mineralogist*, v. 100, p. 1355–1377, doi:10.2138/am-2015-  
745 5134.
- 746 Walters, J.B., Cruz-Uribe, A.M., and Marschall, H.R., 2019, Isotopic compositions of sulfides in  
747 exhumed high-pressure terranes: Implications for sulfur cycling in subduction zones:  
748 *Geochemistry, Geophysics, Geosystems*, p. 2019GC008374, doi:10.1029/2019GC008374.
- 749
- 750

751

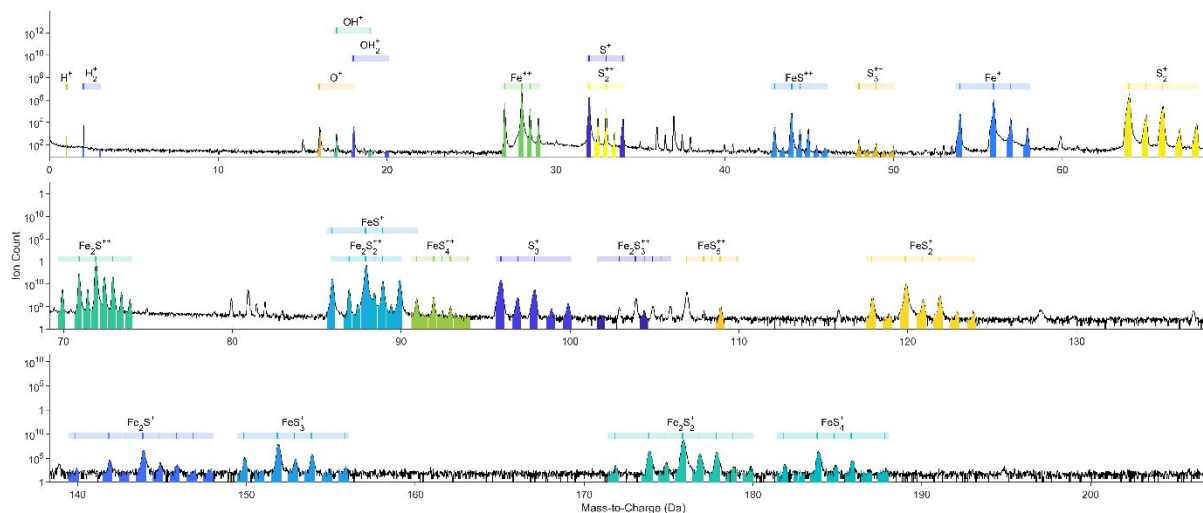
## Figures and Supplementary Materials for

752 **Atom probe tomography for isotopic analysis: development of the  $^{34}\text{S}/^{32}\text{S}$  system in sulfides**

753

754 Phillip Gopon, James O. Douglas, Frederick Meisenkothen, Jaspreet Singh, Andrew London, Michael P. Moody

755

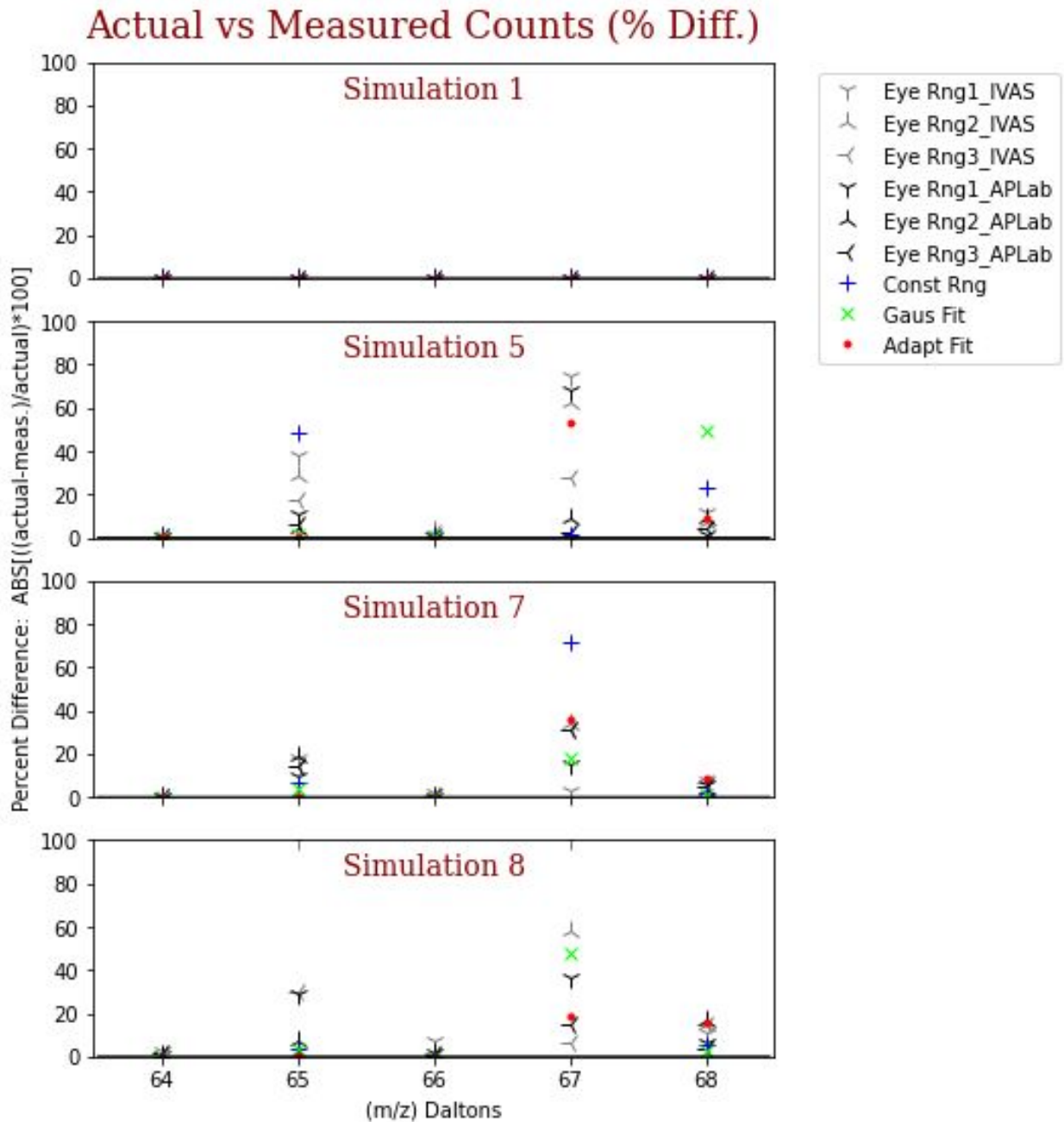


756

757 Figure 1: Mass spectrum of dataset R5083\_08493, showing the complexity of the mass spectrum as well as the  
 758 overlaps present on the main S peak family (34 Da, 33 Da, 34 Da, 36 Da). Note only the main peaks are labeled  
 759 for sake of clarity.

760

761

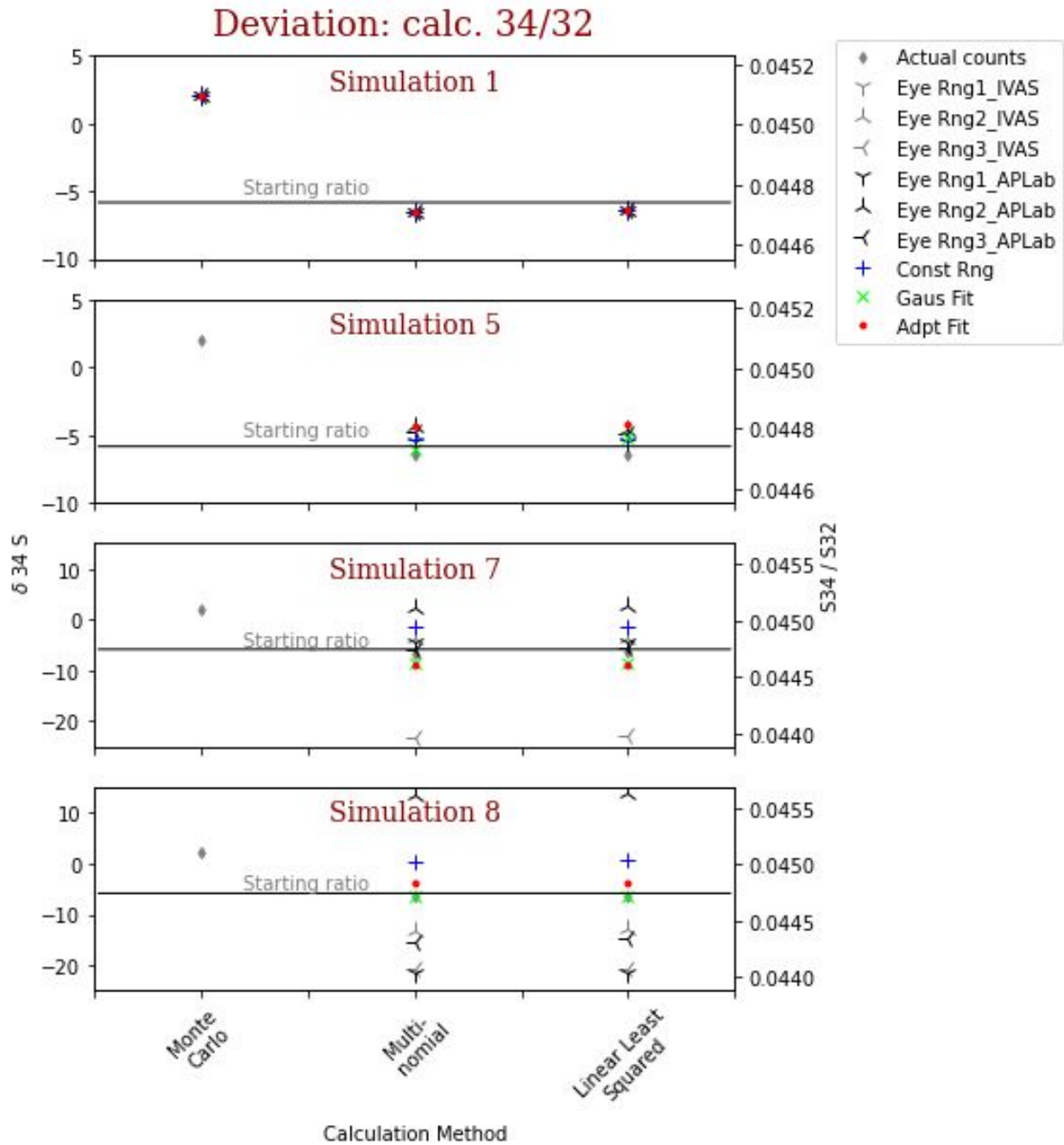


762  
763

Figure 2: Plot of the deviation of the various methods of peak count determination from the 'actual.' Note values

764

shown are absolute values of percent differences calculated from the values in Table 1.



765

766

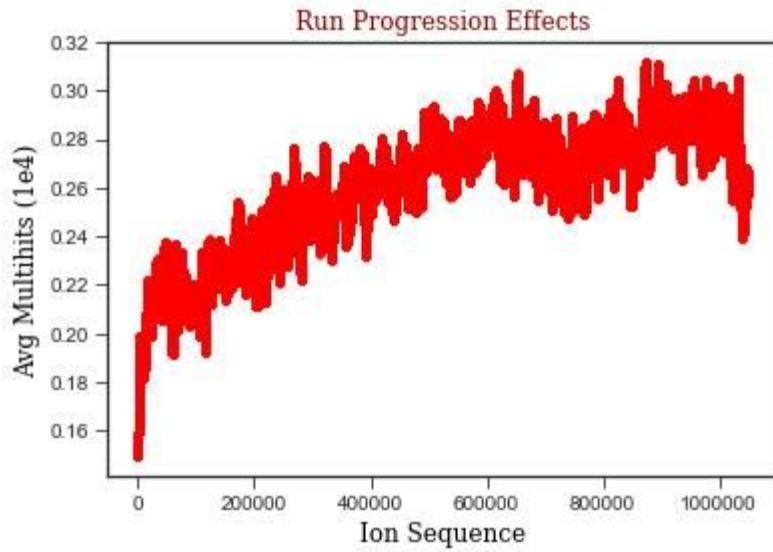
767

768

769

770

Figure 3: Comparison of three different methods to determine the  $^{34}\text{S}/^{32}\text{S}$  ratios (from Table 1). Plotted as both  $\delta^{34}\text{S}$  (left axis) and absolute  $^{34}\text{S}/^{32}\text{S}$  ratio (right axis). Note that only  $\pm 20\%$   $\delta^{34}\text{S}$  is shown. Values outside of this range can be found in Table 1. With the exception of Simulation 1, all calculations using the Monte Carlo Approach are outside of this range.



771

772

773

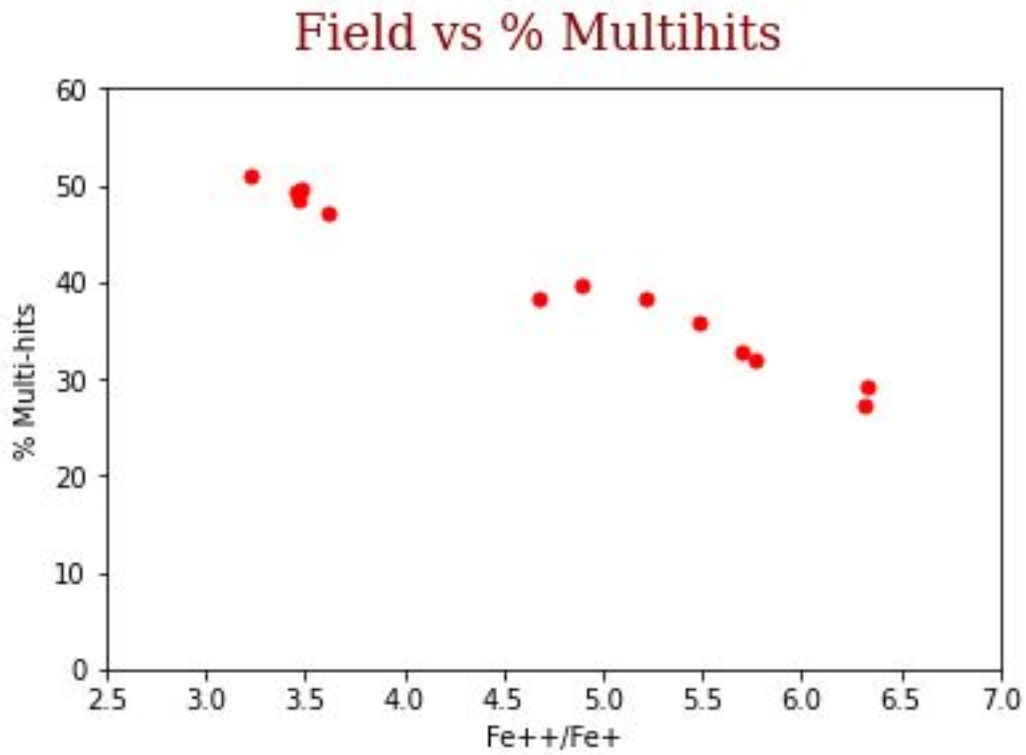
774

775

776

Figure 4: The ion hit sequence plotted versus multi-hits (averaged over  $1e^4$  ion hits) for dataset R5083\_08493. Note the increase in multi-hits as the run progresses.

777



778

779 Figure 5: Plot of % multi-hits versus the charge state ratio of Fe<sup>++</sup>/Fe<sup>+</sup> (from Table 2). The CSR is used here as a  
780 direct proxy for the local electric field.

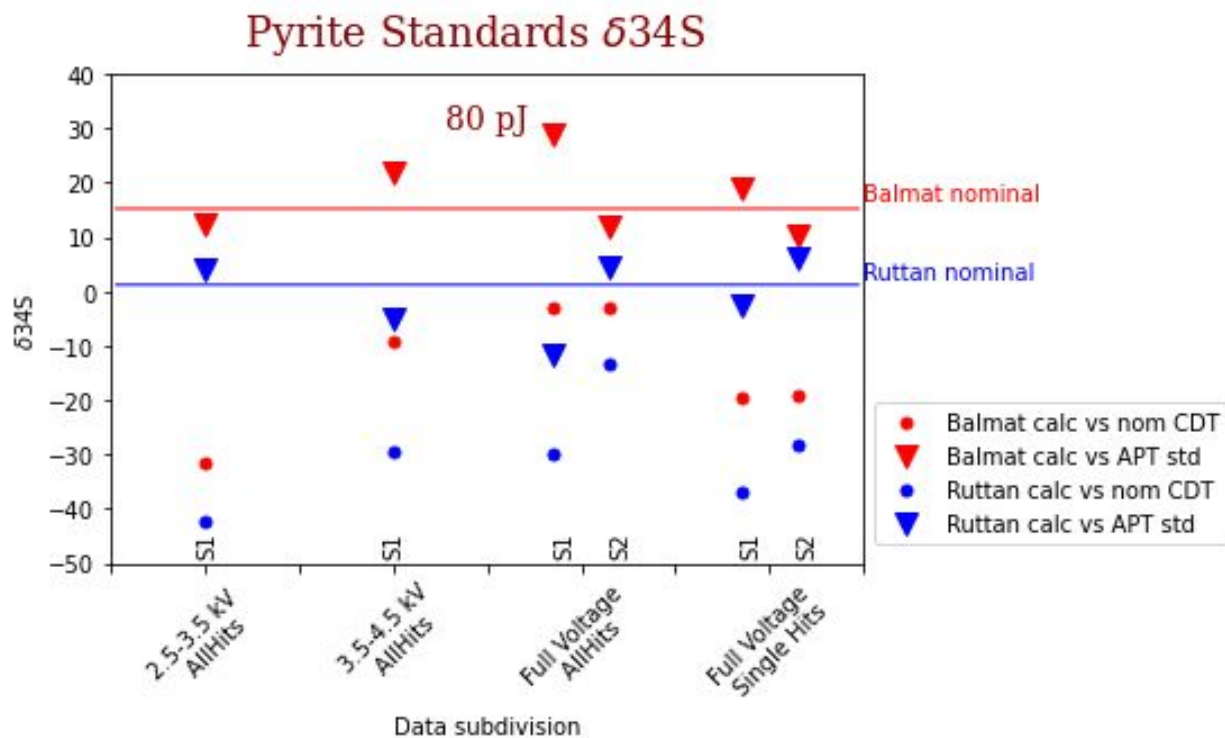


Figure 6: Comparison of calculated  $\delta^{34}\text{S}$  of datasets of pyrite standards run at 80 pJ. Data is subdivided by specific voltage ranges, as well as if only single hits or all hits are used. S1 means dataset pair 08492/08493 and S2 dataset pair 11434/11435. Data is shown both calculated against the nominal CDT value (Equation 8) and against a known standard (Equation 9).

		Intensities Normalized to 1					d34S	d34S	d34S	d34S	
Starting <sup>1</sup> d34S = -5.84		64 counts	65 counts	66 counts	67 counts	68 counts	Monte Carlo	Multinomial	Linear L.S.	Actual	
Simulation	Peak cnt method	Bkg method									
Sim 1	<i>Actual</i>	<i>none need</i>	0.902318	0.014295	0.080746	0.000649	0.001993	2.05	-6.50	-6.39	-5.84
	Eye Rangir.	1 IVAS	0.902318	0.014295	0.080746	0.000649	0.001993	2.05	-6.50	-6.39	-5.84
		1 APT Lab	0.902318	0.014295	0.080746	0.000649	0.001993	2.05	-6.50	-6.39	-5.84
		2 IVAS	0.902318	0.014295	0.080746	0.000649	0.001993	2.05	-6.50	-6.39	-5.84
	Eye Rangir.	2 APT Lab	0.902318	0.014295	0.080746	0.000649	0.001993	2.05	-6.50	-6.39	-5.84
		3 IVAS	0.902318	0.014295	0.080746	0.000649	0.001993	2.05	-6.50	-6.39	-5.84
		3 APT Lab	0.902318	0.014295	0.080746	0.000649	0.001993	2.05	-6.50	-6.39	-5.84
	Constant Range	IVAS	0.902318	0.014295	0.080746	0.000649	0.001993	2.05	-6.50	-6.39	-5.84
	Gaussian Fit (FWHM)	linear									
	Adapt. pk fit	constant	0.902318	0.014295	0.080746	0.000649	0.001992	2.05	-6.50	-6.39	-5.84
Sim 5	<i>Actual</i>	<i>none need</i>	0.902241	0.014246	0.080888	0.000637	0.001988	-6.99	-4.56	-4.56	-5.84
	Eye Rangir.	1 IVAS	0.909896	0.008771	0.079416	0.000159	0.001758	-374.50	-30.58	-30.58	-5.84
		1 APT Lab	0.904224	0.012633	0.080984	0.000202	0.001957	-405.15	-5.51	-5.45	-5.84
		2 IVAS	0.896353	0.018281	0.083278	0.000241	0.001847	-450.54	31.05	30.93	-5.84
	Eye Rangir.	2 APT Lab	0.902948	0.013682	0.080968	0.000583	0.001819	-30.12	-4.39	-4.56	-5.84
		3 IVAS	0.899317	0.011750	0.082903	0.000462	0.005567	-54.31	23.70	25.94	-5.84
		3 APT Lab	0.902915	0.013428	0.080938	0.000652	0.002067	35.44	-4.71	-4.97	-5.84
	Constant Range	APT Lab	0.909017	0.007384	0.081416	0.000646	0.001538	-35.42	-5.26	-5.26	-5.84
	Gaussian Fit (FWHM)	linear	0.899611	0.014020	0.080536	0.002865	0.002968	498.87	-6.07	-5.14	-5.84
	Adapt. pk fit	constant	0.901776	0.014219	0.080868	0.000976	0.002161	138.28	-4.39	-4.16	-5.84
Sim 7	<i>Actual</i>	<i>none need</i>	0.902460	0.014241	0.080673	0.000634	0.001993	-9.24	-7.54	-7.44	-5.84
	Eye Rangir.	1 IVAS	0.907144	0.011612	0.078783	0.000615	0.001846	25.22	-35.58	-35.50	-5.84
		1 APT Lab	0.901137	0.015628	0.080816	0.000540	0.001880	-125.67	-4.46	-4.44	-5.84
		2 IVAS	0.901757	0.014547	0.080936	0.000848	0.001912	51.43	-3.56	-3.49	-5.84
	Eye Rangir.	2 APT Lab	0.898424	0.016973	0.081144	0.001403	0.002055	128.74	2.45	2.65	-5.84
		3 IVAS	0.905754	0.012250	0.079690	0.000439	0.001867	-117.74	-23.02	-22.97	-5.84
		3 APT Lab	0.900747	0.016228	0.080688	0.000433	0.001904	-250.04	-5.77	-5.65	-5.84
	Constant Range	APT Lab	0.900630	0.015232	0.081010	0.001087	0.002040	109.90	-1.47	-1.31	-5.84
	Gaussian Fit (FWHM)	linear	0.901866	0.014815	0.080547	0.000750	0.002023	56.23	-8.50	-8.37	-5.84
	Adapt. pk fit	constant	0.902954	0.014207	0.080616	0.000406	0.001818	-206.51	-8.78	-8.79	-5.84
Sim 8	<i>Actual</i>	<i>none need</i>	0.902231	0.014208	0.080908	0.000650	0.002003	5.92	-4.39	-4.28	-5.84
	Eye Rangir.	1 IVAS	0.923023	0.000000	0.075205	0.000000	0.001772	6026.58	-94.79	-94.67	-5.84
		1 APT Lab	0.899390	0.018292	0.079301	0.000886	0.002131	26.93	-21.56	-21.34	-5.84
		2 IVAS	0.902490	0.013977	0.080214	0.001025	0.002294	186.90	-13.20	-12.88	-5.84
	Eye Rangir.	2 APT Lab	0.897537	0.015237	0.081935	0.002959	0.002333	305.70	13.42	13.97	-5.84
		3 IVAS	0.899880	0.018396	0.079418	0.000607	0.001699	-153.34	-20.66	-20.71	-5.84
		3 APT Lab	0.917043	-0.001202	0.081329	0.000747	0.002083	52.35	-15.42	-14.52	-5.84
	Constant Range	APT Lab	0.899972	0.014690	0.081083	0.002134	0.002122	207.92	0.22	0.56	-5.84
	Gaussian Fit (FWHM)	linear	0.902500	0.013727	0.080761	0.000960	0.002052	109.90	-6.45	-6.28	-5.84
	Adapt. pk fit	constant	0.902706	0.014085	0.080993	0.000528	0.001688	-91.25	-3.86	-3.94	-5.84

Table 1: Collation of various methods used to measure peak counts and to calculate the  $^{34}\text{S}/^{32}\text{S}$  ratio. To save space, only Simulations 1,5,7,8 are shown. Results for all simulations are reported in Appendix C.



							Standard	Mineral	Formula	$^{34}\text{S}/^{32}\text{S}$	$\delta^{34}\text{S}$ (CDT)
Canyon Diablo Troilite							Canyon Diablo	Troilite	FeS	0.045005	0
Ruttan Pyrite							Ruttan	Pyrite	FeS <sub>2</sub>	0.045059	1.2
Balmat Pyrite							Balmat	Pyrite	FeS <sub>2</sub>	0.045684	15.1

80 pJ, Varying Ion Ratio	Ions e6	Instrument	Standard	Cond.	Dataset	Voltage Range	Fe <sup>++</sup> /Fe <sup>+</sup>	% Multihits	Data type	$^{34}\text{S}/^{32}\text{S}$	$\delta^{34}\text{S}$ (model CDT)	$\delta^{34}\text{S}$ (APT Stand)
Balmat_XR_8493_80pJ_2500-3500V_allHits	61	LEAP 5000-XR	Balmat	80pJ	08493	2500-3500V	6.33	29.19	all hits	0.043578	-32	12
Balmat_XR_8493_80pJ_3500_4500V_allHits	61	LEAP 5000-XR	Balmat	80pJ	08493	3500-4500V	5.49	35.89	all hits	0.044582	-9	22
Balmat_XR_8493_80pJ_fullvoltage_allHits	61	LEAP 5000-XR	Balmat	80pJ	08493	Full voltage	5.21	38.43	all hits	0.044872	-3	29
Balmat_XR_8493_80pJ_fullvoltage_singleHits		LEAP 5000-XR	Balmat	80pJ	08493	Full voltage			single hits	0.044118	-20	19
Balmat_XR_11434_80pJ_fullvoltage_allHits		LEAP 5000-XR	Balmat	80pJ	11434	Full voltage	4.89	39.69	all hits	0.044871	-3	12
Balmat_XR_11434_80pJ_fullvoltage_singleHits		LEAP 5000-XR	Balmat	80pJ	11434	Full voltage			single hits	0.044134	-19	10
Ruttan_XR_8492_80pJ_2500-3500V_allHits	25	LEAP 5000-XR	Ruttan	80pJ	08492	2500-3500V	6.32	27.29	all hits	0.043099	-42	4
Ruttan_XR_8492_80pJ_3500-4500V_allHits	25	LEAP 5000-XR	Ruttan	80pJ	08492	3500-4500V	5.7	32.81	all hits	0.043684	-29	-5
Ruttan_XR_8492_80pJ_fullvoltage_allHits	25	LEAP 5000-XR	Ruttan	80pJ	08492	Full Voltage	5.77	32.06	all hits	0.043665	-30	-12
Ruttan_XR_8492_80pJ_fullvoltage_singleHits		LEAP 5000-XR	Ruttan	80pJ	08492	Full Voltage			single hits	0.043341	-37	-2
Ruttan_XR_11435_80pJ_fullvoltage_allHits		LEAP 5000-XR	Ruttan	80pJ	11435	Full Voltage	4.68	38.23	all hits	0.044395	-14	4
Ruttan_XR_11435_80pJ_fullvoltage_singleHits		LEAP 5000-XR	Ruttan	80pJ	11435	Full Voltage			single hits	0.043732	-28	6

40 pJ, Varying Ion Ratio	Ions e6	Instrument	Standard	Cond.	Dataset	Voltage Range	Fe <sup>++</sup> /Fe <sup>+</sup>	% Multihits	Data type	$^{34}\text{S}/^{32}\text{S}$	$\delta^{34}\text{S}$ (model CDT)	$\delta^{34}\text{S}$ (APT Stand)
Balmat_XR_8462_40pJ_full_voltage_allHits	33	LEAP 5000-XR	Balmat	40pJ	08462	Full Voltage	3.23	51.09	all hits	0.045822	18	15
Balmat_XR_8462_40pJ_fullvoltage_singleHits		LEAP 5000-XR	Balmat	40pJ	08462	Full Voltage			single hits	0.044802	-5	17
Balmat_XR_8460_40pJ_fullvoltage_allHits	20	LEAP 5000-XR	Balmat	40pJ	08460	Full Voltage	3.48	49.73	all hits	0.045561	12	9
Balmat_XR_8460_40pJ_fullvoltage_singleHits		LEAP 5000-XR	Balmat	40pJ	08460	Full Voltage			single hits	0.044549	-10	11
Ruttan_XR_8458_40pJ_fullvoltage_allHits	16	LEAP 5000-XR	Ruttan	40pJ	08458	Full Voltage	3.47	48.54	all hits	0.045188	4	1
Ruttan_XR_8458_40pJ_fullvoltage_singleHits		LEAP 5000-XR	Ruttan	40pJ	08458	Full Voltage			single hits	0.044121	-20	0

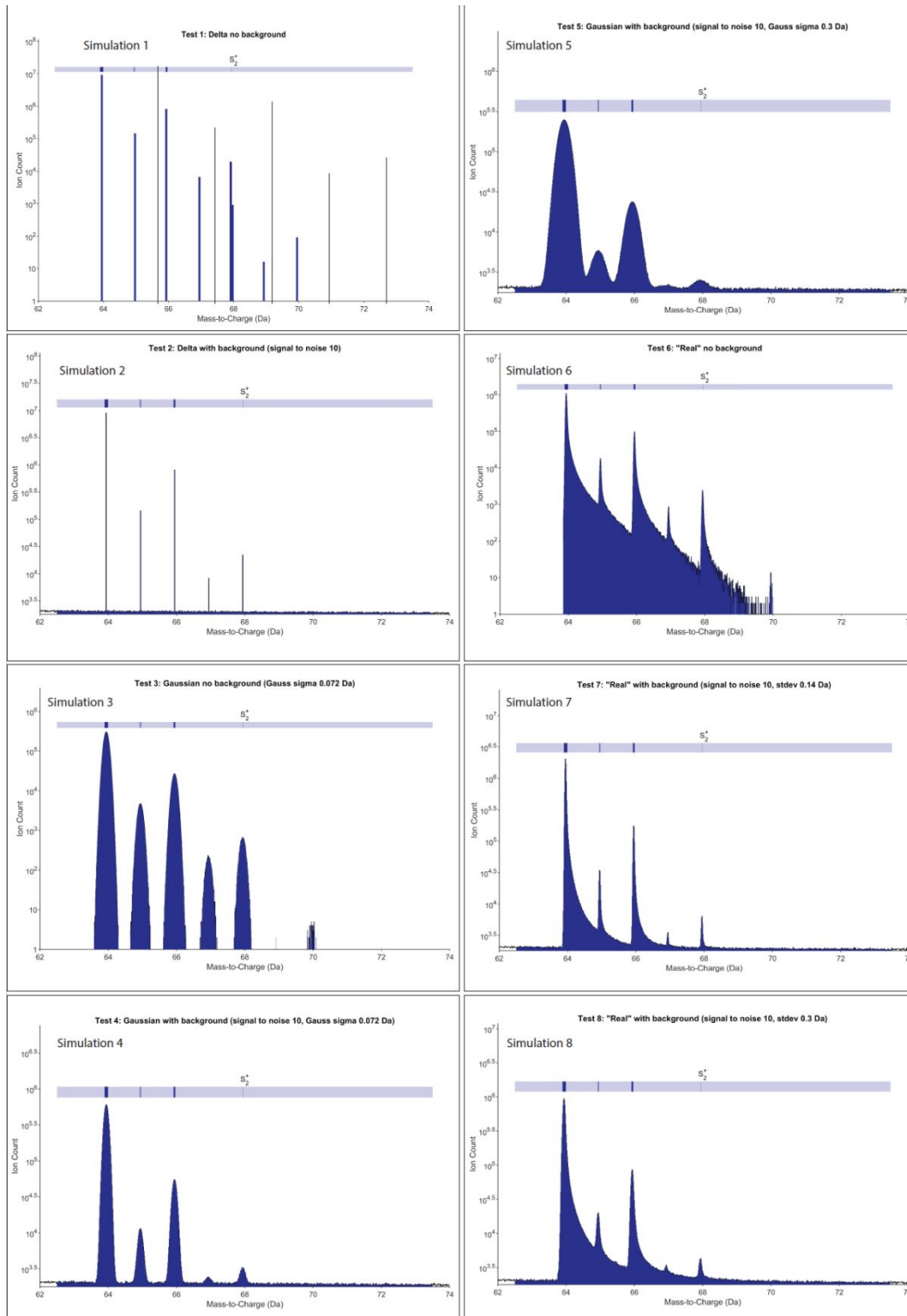
80 pJ, Constant Ion Ratio, $^{34}\text{S}^{+1}/^{32}\text{S}_2^{+1} = 1:1$	Ions e6	Instrument	Standard	Cond.	Dataset	Voltage Range	Fe <sup>++</sup> /Fe <sup>+</sup>	% Multihits	Data type	$^{34}\text{S}/^{32}\text{S}$	$\delta^{34}\text{S}$ (model CDT)	$\delta^{34}\text{S}$ (APT Stand)
Balmat_XR_9023_fullvoltage_allHits	26	LEAP 5000-XR	Balmat	S <sup>+</sup> /S <sub>2</sub> <sup>+</sup> =1:1	09023	Full Voltage	3.46	49.23	all hits	0.045829	18	22
Balmat_XR_9023_fullvoltage_singleHits		LEAP 5000-XR	Balmat	S <sup>+</sup> /S <sub>2</sub> <sup>+</sup> =1:1	09023	Full Voltage			single hits	0.044806	-4	24
Ruttan_XR_9021_fullvoltage_allHits	20	LEAP 5000-XR	Ruttan	S <sup>+</sup> /S <sub>2</sub> <sup>+</sup> =1:1	09021	Full Voltage	3.62	47.1	all hits	0.044894	-2	-5
Ruttan_XR_9021_fullvoltage_singleHits		LEAP 5000-XR	Ruttan	S <sup>+</sup> /S <sub>2</sub> <sup>+</sup> =1:1	09021	Full Voltage			single hits	0.043822	-26	-7

Table 2: Run conditions, calculated  $^{34}\text{S}/^{32}\text{S}$ , and  $\delta^{34}\text{S}$  for each dataset and subdivision of each dataset. Multi-hit fractions as well as the corresponding Fe<sup>++</sup>/Fe<sup>+</sup> ratio (as a proxy for the local field), were calculated for the data containing all hits.  $\delta^{34}\text{S}$  is calculated both against the nominal CDT value (equation (8)) and calculated against the corresponding standard that was acquired closest in time (equation (9)). Note - other than applied voltage, all other acquisition conditions kept constant (see section 2).

**Appendix A: Detailed table of all ranges used for the ranging exercise.**

Analyst #	Sim. #	64 Da		65 Da		66 Da		67 Da	
		Start	End	Start	End	Start	End	Start	End
User 1	1	63.8440	64.1440	64.8440	65.1440	65.8400	66.1400	66.8390	67.1390
User 2	1	63.5510	64.3330	64.5520	65.3340	65.5500	66.3320	66.5440	67.3260
User 3	1	63.9160	63.9730	64.9250	64.9610	65.9130	65.9680	66.9180	66.9610
User 1	2	63.9350	63.9540	64.9390	64.9520	65.9270	65.9510	66.9240	66.9520
User 2	2	63.5510	64.3330	64.5520	65.3340	65.5500	66.3320	66.5440	67.3260
User 3	2	63.9200	63.9730	64.9250	64.9610	65.9130	65.9680	66.9180	66.9610
User 1	3	63.5580	64.3470	64.6080	65.3100	65.5780	66.3360	66.6460	67.2310
User 2	3	63.5510	64.3330	64.5520	65.3340	65.5500	66.3320	66.5440	67.3260
User 3	3	63.4920	64.3640	64.5570	65.3430	65.5450	66.3820	66.5980	67.3450
User 1	4	63.6090	64.2890	64.7040	65.2060	65.6590	66.2450	66.7030	67.1460
User 2	4	63.5650	64.3040	64.5890	65.2550	65.5210	66.2670	66.6140	67.2420
User 3	4	63.4740	64.3500	64.6350	65.2820	65.5870	66.3160	66.7130	67.1660
User 1	5	63.1760	64.5910	64.6270	65.3560	65.4010	66.5960	66.7500	67.1510
User 2	5	63.2990	64.5500	64.5500	65.3440	65.3540	66.5050	66.6840	67.2790
User 3	5	63.0550	64.5830	64.5990	65.3420	65.3690	66.5410	66.6040	67.3400
User 1	6	63.8550	64.8050	64.8790	65.8200	65.8640	66.8260	66.8930	67.7270
User 2	6	63.6590	64.2340	64.6570	65.2320	65.7720	66.3470	66.6540	67.2290
User 3	6	63.7920	64.8140	64.8430	65.7600	65.7890	66.8020	66.8380	67.7020
User 1	7	63.8670	64.8500	64.8880	65.6280	65.8680	66.8610	66.8850	67.0550
User 2	7	63.6590	64.2340	64.6570	65.2320	65.6610	66.2360	66.6540	67.2290
User 3	7	63.7790	64.8130	64.8550	65.7790	65.8380	66.6850	66.8380	67.0750
User 1	8	63.7520	64.8380	64.8570	65.7930	65.8230	66.8010	66.8270	67.2140
User 2	8	63.6590	64.2340	64.6570	65.2320	65.6610	66.2360	66.6540	67.2290
User 3	8	63.6770	64.7850	64.7930	65.6400	65.7350	66.6850	66.8200	67.0580

## Appendix B: Simulated spectra (Simulations 1-8)



## Appendix C: Full simulated data results (Simulations 1-8)

		normalized to 1					d34s	d34s	d34s	d34s		
Simulation	Peak cnt method	Bkg method	64 counts	65 counts	66 counts	67 counts	68 counts	Monte Carlo	Multinomial	Linear Lst. Sqr.	Actual	
Sim 1	Actual	none need	0.902318	0.014295	0.080746	0.000649	0.001993	2.05	-6.50	-6.39	-5.84	
		1 IVAS	0.902318	0.014295	0.080746	0.000649	0.001993	2.05	-6.50	-6.39	-5.84	
		1 APT Lab	0.902318	0.014295	0.080746	0.000649	0.001993	2.05	-6.50	-6.39	-5.84	
		2 IVAS	0.902318	0.014295	0.080746	0.000649	0.001993	2.05	-6.50	-6.39	-5.84	
		2 APT Lab	0.902318	0.014295	0.080746	0.000649	0.001993	2.05	-6.50	-6.39	-5.84	
		3 IVAS	0.902318	0.014295	0.080746	0.000649	0.001993	2.05	-6.50	-6.39	-5.84	
		3 APT Lab	0.902318	0.014295	0.080746	0.000649	0.001993	2.05	-6.50	-6.39	-5.84	
		Constant Range	IVAS	0.902318	0.014295	0.080746	0.000649	0.001993	2.05	-6.50	-6.39	-5.84
		Gaussian Fit (FWHM)	linear									
		Adapt. pk fit	constant	0.902318	0.014295	0.080746	0.000649	0.001992	2.05	-6.50	-6.39	-5.84
Sim 2	Actual	none need	0.902422	0.014211	0.080738	0.000625	0.002005	-15.39	-6.69	-6.58	-5.84	
		1 IVAS	0.902408	0.014210	0.080731	0.000639	0.002012	-4.75	-6.77	-6.65	-5.84	
		1 APT Lab	0.902404	0.014213	0.080739	0.000635	0.002009	-8.50	-6.67	-6.55	-5.84	
		2 IVAS	0.902524	0.014143	0.080741	0.000591	0.002001	-38.27	-6.76	-6.66	-5.84	
		2 APT Lab	0.902448	0.014175	0.080744	0.000627	0.002006	-10.86	-6.65	-6.54	-5.84	
		3 IVAS	0.902400	0.014221	0.080727	0.000638	0.002014	-4.75	-6.81	-6.70	-5.84	
		3 APT Lab	0.902410	0.014218	0.080727	0.000634	0.002011	-7.77	-6.82	-6.71	-5.84	
		Constant Range	APT Lab	0.902482	0.014191	0.080716	0.000631	0.001980	-9.39	-7.03	-6.93	-5.84
		Gaussian Fit (FWHM)	linear									
		Adapt. pk fit	constant	0.902421	0.014209	0.080738	0.000625	0.002007	-15.42	-6.70	-6.58	-5.84
Sim 3	Actual	none need	0.902088	0.014277	0.080980	0.000647	0.002007	0.58	-3.25	-3.25	-5.84	
		1 IVAS	0.902088	0.014277	0.080980	0.000647	0.002007	0.58	-3.36	-3.25	-5.84	
		1 APT Lab	0.902088	0.014277	0.080980	0.000647	0.002007	0.58	-3.36	-3.25	-5.84	
		2 IVAS	0.902088	0.014277	0.080980	0.000647	0.002007	0.58	-3.36	-3.25	-5.84	
		2 APT Lab	0.902088	0.014277	0.080980	0.000647	0.002007	0.58	-3.36	-3.25	-5.84	
		3 IVAS	0.902088	0.014277	0.080980	0.000647	0.002007	0.58	-3.36	-3.25	-5.84	
		3 APT Lab	0.902088	0.014277	0.080980	0.000647	0.002007	0.58	-3.36	-3.25	-5.84	
		Constant Range	APT Lab	0.902117	0.014279	0.080987	0.000630	0.001987	-11.55	-3.20	-3.20	-5.84
		Gaussian Fit (FWHM)	linear	0.902025	0.014170	0.081122	0.000713	0.001970	49.80	-1.53	-1.44	-5.84
		Adapt. pk fit	constant	0.902080	0.014267	0.080996	0.000644	0.002012	-0.93	-3.14	-3.04	-5.84
Sim 4	Actual	none need	0.902446	0.014211	0.080714	0.000638	0.001991	-4.80	-6.92	-6.92	-5.84	
		1 IVAS	0.902193	0.014116	0.080870	0.000884	0.001937	65.06	-4.81	-4.72	-5.84	
		1 APT Lab	0.902445	0.014228	0.080727	0.000633	0.001968	-9.24	-6.86	-6.77	-5.84	
		2 IVAS	0.902178	0.014191	0.080601	0.000611	0.002420	-27.15	-8.12	-7.77	-5.84	
		2 APT Lab	0.902463	0.014226	0.080724	0.000624	0.001964	-16.81	-6.92	-6.83	-5.84	
		3 IVAS	0.901436	0.015010	0.080618	0.000841	0.002096	100.59	-7.18	-6.99	-5.84	
		3 APT Lab	0.902450	0.014245	0.080702	0.000629	0.001974	-11.55	-7.18	-7.09	-5.84	
		Constant Range	APT Lab	0.902525	0.014235	0.080667	0.000638	0.001934	-6.28	-7.61	-7.61	-5.84
		Gaussian Fit (FWHM)	linear	0.901900	0.014230	0.080648	0.001088	0.002134	142.42	-7.24	-7.01	-5.84
		Adapt. pk fit	constant	0.902462	0.014203	0.080639	0.000686	0.002010	31.55	-7.97	-7.84	-5.84
Sim 5	Actual	none need	0.902240644	0.014245654	0.080887974	0.000637407	0.001988321	-6.99	-4.56	-4.56	-5.84	
		1 IVAS	0.909896005	0.008771452	0.079415592	0.000158689	0.001758262	-374.50	-30.58	-30.58	-5.84	
		1 APT Lab	0.904223641	0.012632921	0.080984269	0.000202283	0.001956886	-405.15	-5.51	-5.45	-5.84	
		2 IVAS	0.896352719	0.018280659	0.083277856	0.000241392	0.001847374	-450.54	31.05	30.93	-5.84	
		2 APT Lab	0.902947924	0.013682173	0.080968127	0.000582662	0.001819114	-30.12	-4.39	-4.56	-5.84	
		3 IVAS	0.899317377	0.011749941	0.082903092	0.000462345	0.005567246	-54.31	23.70	25.94	-5.84	
		3 APT Lab	0.902915142	0.013427944	0.080937738	0.000652279	0.002066897	35.44	-4.71	-4.97	-5.84	
		Constant Range	APT Lab	0.909017022	0.007383716	0.08141581	0.000645522	0.001537993	-35.42	-5.26	-5.26	-5.84
		Gaussian Fit (FWHM)	linear	0.899611134	0.014019648	0.080536226	0.00286533	0.002967663	498.87	-6.07	-5.14	-5.84
		Adapt. pk fit	constant	0.90177589	0.014218601	0.080868008	0.0009763	0.0021612	138.28	-4.39	-4.16	-5.84
Sim 6	Actual	none need	0.902257542	0.01432024	0.080775192	0.000630706	0.00201632	-11.55	-6.07	-5.95	-5.84	
		1 IVAS	0.904698878	0.013849068	0.07958078	0	0.001871275	6026.58	-23.37	-23.36	-5.84	
		1 APT Lab	0.902115099	0.014794896	0.080616698	0.000509313	0.001963994	-129.77	-7.91	-7.83	-5.84	
		2 IVAS	0.90183008	0.013778033	0.081791287	0.00060253	0.001998069	-10.08	6.97	7.05	-5.84	
		2 APT Lab	0.900050043	0.015481984	0.081631215	0.000824572	0.002012186	70.05	6.81	6.92	-5.84	
		3 IVAS	0.904428247	0.011759052	0.081079572	0.000832052	0.001901077	64.29	-4.49	-4.42	-5.84	
		3 APT Lab	0.901691875	0.01479123	0.080797228	0.000756773	0.001962893	52.22	-5.22	-5.13	-5.84	
		Constant Range	APT Lab	0.901936679	0.01456112	0.080786913	0.000696181	0.002019107	27.64	-5.60	-5.47	-5.84
		Gaussian Fit (FWHM)	linear	0.902346545	0.01417704	0.080817475	0.000631945	0.002026995	-7.00	-5.63	-5.51	-5.84
		Adapt. pk fit	constant	0.9023554	0.0142861	0.0808003	0.0005821	0.0019761	-49.19	-5.86	-5.78	-5.84
Sim 7	Actual	none need	0.902459947	0.014240854	0.080672871	0.000633507	0.001992822	-9.24	-7.54	-7.44	-5.84	
		1 IVAS	0.907144186	0.011611837	0.078783121	0.000614797	0.001846058	25.22	-35.58	-35.50	-5.84	
		1 APT Lab	0.901136939	0.015627867	0.080816169	0.000539522	0.001879502	-125.67	-4.46	-4.44	-5.84	
		2 IVAS	0.90175425	0.014547371	0.080935854	0.000847723	0.001911627	51.43	-3.56	-3.49	-5.84	
		2 APT Lab	0.898424369	0.016973062	0.081144263	0.001402908	0.002055397	128.74	2.45	2.65	-5.84	
		3 IVAS	0.905754204	0.012249865	0.079690481	0.000438719	0.001866731	-117.74	-23.02	-22.97	-5.84	
		3 APT Lab	0.900746834	0.016228182	0.080688158	0.000433215	0.001903611	-250.04	-5.77	-5.65	-5.84	
		Constant Range	APT Lab	0.900630342	0.015232457	0.081009779	0.00108739	0.002040033	109.90	-1.47	-1.31	-5.84
		Gaussian Fit (FWHM)	linear	0.901865823	0.014814727	0.080546895	0.000749661	0.002022894	56.23	-8.50	-8.37	-5.84
		Adapt. pk fit	constant	0.9029538	0.0142065	0.0806164	0.0004058	0.0018175	-206.51	-8.78	-8.79	-5.84
Sim 8	Actual	none need	0.902230583	0.014207948	0.080908341	0.000649907	0.002003221	5.92	-4.39	-4.28	-5.84	
		1 IVAS	0.9230227	0	0.075205287	0	0.001772013	6026.58	-94.79	-94.67	-5.84	
		1 APT Lab	0.899390327	0.018292039	0.079300768	0.000886182	0.002130684	26.93	-21.56	-21.34	-5.84	
		2 IVAS	0.902490243	0.013976857	0.080213999	0.001025285	0.002293624	186.90	-13.20	-12.88	-5.84	
		2 APT Lab	0.897536586	0.015236924	0.081934901	0.002959021	0.002332568	305.70	13.42	13.97	-5.84	
		3 IVAS	0.899880424	0.018395772	0.07941766	0.000607485	0.00169866	-153.34	-20.66	-20.71	-5.84	
		3 APT Lab	0.917042553	-0.001201579	0.081328999	0.000747022	0.002083005	52.35	-15.42	-14.52	-5.84	
		Constant Range	APT Lab	0.899971558	0.014689764	0.081083317	0.00213386	0.002121501	207.92	0.22	0.56	-5.84
		Gaussian Fit (FWHM)	linear	0.902500133	0.013726744	0.080761235	0.000959539	0.002052348	109.90	-6.45	-6.28	-5.84
		Adapt. pk fit	constant	0.902706	0.014085	0.0809931	0.0005276	0.0016883	-91.25	-3.86	-3.94	-5.84

## Appendix D: Full empirical data results (Adaptive fit, IVAS, and Gaussian)

### Adaptive Peak Fitting

										Standard	Mineral	Formula	<sup>34</sup> S/ <sup>32</sup> S	δ <sup>34</sup> S (CDT)
Canyon Diablo Troilite										Canyon Diablo	Troilite	FeS	0.045005	0
Ruttan Pyrite										Ruttan	Pyrite	FeS2	0.045059	1.2
Balmat Pyrite										Balmat	Pyrite	FeS2	0.045684	15.1

80 pJ, Varying Ion Ratio	Ions e6	Instrument	Standard	Cond.	Dataset	Voltage Range	Fe <sup>2+</sup> /Fe <sup>+</sup>	% Multihits	Data type	<sup>34</sup> S/ <sup>32</sup> S	δ <sup>34</sup> S (model CDT)	δ <sup>34</sup> S (APT Stand)
Balmat_XR_8493_80pJ_2500-3500V_allHits	61	LEAP 5000-XR	Balmat	80pJ	08493	2500-3500V	6.33	29.19	all hits	0.043578	-32	12
Balmat_XR_8493_80pJ_3500_4500V_allHits	61	LEAP 5000-XR	Balmat	80pJ	08493	3500-4500V	5.49	35.89	all hits	0.044582	-9	22
Balmat_XR_8493_80pJ_fullvoltage_allHits	61	LEAP 5000-XR	Balmat	80pJ	08493	Full voltage	5.21	38.43	all hits	0.044872	-3	29
Balmat_XR_8493_80pJ_fullvoltage_singleHits		LEAP 5000-XR	Balmat	80pJ	08493	Full voltage			single hits	0.044118	-20	19
Balmat_XR_11434_80pJ_fullvoltage_allHits		LEAP 5000-XR	Balmat	80pJ	11434	Full voltage	4.89	39.69	all hits	0.044871	-3	12
Balmat_XR_11434_80pJ_fullvoltage_singleHits		LEAP 5000-XR	Balmat	80pJ	11434	Full voltage			single hits	0.044134	-19	10
Ruttan_XR_8492_80pJ_2500-3500V_allHits	25	LEAP 5000-XR	Ruttan	80pJ	08492	2500-3500V	6.32	27.29	all hits	0.043099	-42	4
Ruttan_XR_8492_80pJ_3500-4500V_allHits	25	LEAP 5000-XR	Ruttan	80pJ	08492	3500-4500V	5.7	32.81	all hits	0.043684	-29	-5
Ruttan_XR_8492_80pJ_fullvoltage_allHits	25	LEAP 5000-XR	Ruttan	80pJ	08492	Full Voltage	5.77	32.06	all hits	0.043665	-30	-12
Ruttan_XR_8492_80pJ_fullvoltage_singleHits		LEAP 5000-XR	Ruttan	80pJ	08492	Full Voltage			single hits	0.043341	-37	-2
Ruttan_XR_11435_80pJ_fullvoltage_allHits		LEAP 5000-XR	Ruttan	80pJ	11435	Full Voltage	4.68	38.23	all hits	0.044395	-14	4
Ruttan_XR_11435_80pJ_fullvoltage_singleHits		LEAP 5000-XR	Ruttan	80pJ	11435	Full Voltage			single hits	0.043732	-28	6

40 pJ, Varying Ion Ratio	Ions e6	Instrument	Standard	Cond.	Dataset	Voltage Range	Fe <sup>2+</sup> /Fe <sup>+</sup>	% Multihits	Data type	<sup>34</sup> S/ <sup>32</sup> S	δ <sup>34</sup> S (model CDT)	δ <sup>34</sup> S (APT Stand)
Balmat_XR_8462_40pJ_full_voltage_allHits	33	LEAP 5000-XR	Balmat	40pJ	08462	Full Voltage	3.23	51.09	all hits	0.045822	18	15
Balmat_XR_8462_40pJ_fullvoltage_singleHits		LEAP 5000-XR	Balmat	40pJ	08462	Full Voltage			single hits	0.044802	-5	17
Balmat_XR_8460_40pJ_fullvoltage_allHits	20	LEAP 5000-XR	Balmat	40pJ	08460	Full Voltage	3.48	49.73	all hits	0.045561	12	9
Balmat_XR_8460_40pJ_fullvoltage_singleHits		LEAP 5000-XR	Balmat	40pJ	08460	Full Voltage			single hits	0.044549	-10	11
Ruttan_XR_8458_40pJ_fullvoltage_allHits	16	LEAP 5000-XR	Ruttan	40pJ	08458	Full Voltage	3.47	48.54	all hits	0.045188	4	1
Ruttan_XR_8458_40pJ_fullvoltage_singleHits		LEAP 5000-XR	Ruttan	40pJ	08458	Full Voltage			single hits	0.044121	-20	0

80 pJ, Constant Ion Ratio, <sup>32</sup> S <sup>+</sup> / <sup>32</sup> S <sup>2+</sup> = 1:1	Ions e6	Instrument	Standard	Cond.	Dataset	Voltage Range	Fe <sup>2+</sup> /Fe <sup>+</sup>	% Multihits	Data type	<sup>34</sup> S/ <sup>32</sup> S	δ <sup>34</sup> S (model CDT)	δ <sup>34</sup> S (APT Stand)
Balmat_XR_9023_fullvoltage_allHits	26	LEAP 5000-XR	Balmat	S <sup>+</sup> /S <sup>2+</sup> =1:1	09023	Full Voltage	3.46	49.23	all hits	0.045829	18	22
Balmat_XR_9023_fullvoltage_singleHits		LEAP 5000-XR	Balmat	S <sup>+</sup> /S <sup>2+</sup> =1:1	09023	Full Voltage			single hits	0.044806	-4	24
Ruttan_XR_9021_fullvoltage_allHits	20	LEAP 5000-XR	Ruttan	S <sup>+</sup> /S <sup>2+</sup> =1:1	09021	Full Voltage	3.62	47.1	all hits	0.044894	-2	-5
Ruttan_XR_9021_fullvoltage_singleHits		LEAP 5000-XR	Ruttan	S <sup>+</sup> /S <sup>2+</sup> =1:1	09021	Full Voltage			single hits	0.043822	-26	-7

### IVAS

										Standard	Mineral	Formula	<sup>34</sup> S/ <sup>32</sup> S	δ <sup>34</sup> S (CDT)
Canyon Diablo Troilite										Canyon Diablo	Troilite	FeS	0.045005	0
Ruttan Pyrite										Ruttan	Pyrite	FeS2	0.045059	1.2
Balmat Pyrite										Balmat	Pyrite	FeS2	0.045684	15.1

80 pJ, Varying Ion Ratio	Instrument	Standard	Dataset	Voltage Range	Fe <sup>2+</sup> /Fe <sup>+</sup>	Data type	<sup>34</sup> S/ <sup>32</sup> S	δ <sup>34</sup> S (model CDT)	δ <sup>34</sup> S (Ruttan)
Balmat_XR_8493_80pJ_fullvoltage	LEAP 5000-XR	Balmat	08493	Full voltage	5.21	all hits	0.045565	12	29
Balmat_XR_11434_80pJ_fullvoltage	LEAP 5000-XR	Balmat	11434	Full voltage		all hits	0.045591	13	14
Ruttan_XR_8492_80pJ_fullvoltage	LEAP 5000-XR	Ruttan	08492	Full Voltage	5.77	all hits	0.044334	-15	-12
Ruttan_XR_11435_80pJ_fullvoltage	LEAP 5000-XR	Ruttan	11435	Full Voltage		all hits	0.045015	0	2

40 pJ, Varying Ion Ratio	Instrument	Standard	Dataset	Voltage Range	Fe <sup>2+</sup> /Fe <sup>+</sup>	Data type	<sup>34</sup> S/ <sup>32</sup> S	δ <sup>34</sup> S (model CDT)	δ <sup>34</sup> S (Ruttan)
Balmat_XR_8462_40pJ_full voltage	LEAP 5000-XR	Balmat	08462	Full Voltage	3.23	all hits	0.046207	27	12
Balmat_XR_8460_40pJ_fullvoltage	LEAP 5000-XR	Balmat	08460	Full Voltage	3.48	all hits	0.046123	25	10
Ruttan_XR_8458_40pJ_fullvoltage	LEAP 5000-XR	Ruttan	08458	Full Voltage	3.47	all hits	0.045699	15	4

80 pJ, Constant Ion Ratio, <sup>32</sup> S <sup>+</sup> / <sup>32</sup> S <sup>2+</sup> = 1:1	Instrument	Standard	Dataset	Voltage Range	Fe <sup>2+</sup> /Fe <sup>+</sup>	Data type	<sup>34</sup> S/ <sup>32</sup> S	δ <sup>34</sup> S (model CDT)	δ <sup>34</sup> S (Ruttan)
Balmat_XR_9023_fullvoltage	LEAP 5000-XR	Balmat	09023	Full Voltage	3.46	all hits	0.046126	25	19
Ruttan_XR_9021_fullvoltage	LEAP 5000-XR	Ruttan	09021	Full Voltage	3.62	all hits	0.045317	7	-2

## Gaussian Fitting

	Standard	Mineral	Formula	$^{34}\text{S}/^{32}\text{S}$	$\delta^{34}\text{S}$ (CDT)	
Canyon Diablo Troilite	Canyon Diablo	Troilite	FeS	0.045005	0	
Ruttan Pyrite	Ruttan	Pyrite	FeS <sub>2</sub>	0.045059	1.2	
Balmat Pyrite	Balmat	Pyrite	FeS <sub>2</sub>	0.045684	15.1	

80 pJ, Varying Ion Ratio	Instrument	Standard	Dataset	Voltage Range	Fe <sup>++</sup> /Fe <sup>+</sup>	Data type	$^{34}\text{S}/^{32}\text{S}$	$\delta^{34}\text{S}$ (model CDT)	$\delta^{34}\text{S}$ (Ruttan)
Balmat_XR_8493_80pJ_fullvoltage	LEAP 5000-XR	Balmat	08493	Full voltage	5.21	all hits	0.044105	-20	20
Balmat_XR_8493_80pJ_fullvoltage	LEAP 5000-XR	Balmat	08493	Full voltage		single hits	0.043620	-31	15
Ruttan_XR_8492_80pJ_fullvoltage	LEAP 5000-XR	Ruttan	08492	Full Voltage	5.77	all hits	0.043298	-38	-3
Ruttan_XR_8492_80pJ_fullvoltage	LEAP 5000-XR	Ruttan	08492	Full Voltage		single hits	0.043009	-44	1

40 pJ, Varying Ion Ratio	Instrument	Standard	Dataset	Voltage Range	Fe <sup>++</sup> /Fe <sup>+</sup>	Data type	$^{34}\text{S}/^{32}\text{S}$	$\delta^{34}\text{S}$ (model CDT)	$\delta^{34}\text{S}$ (Ruttan)
Balmat_XR_8462_40pJ_full voltage	LEAP 5000-XR	Balmat	08462	Full Voltage	3.23	all hits	0.044596	-9	8
Balmat_XR_8462_40pJ_fullvoltage	LEAP 5000-XR	Balmat	08462	Full Voltage		single hits	0.044261	-17	11
Balmat_XR_8460_40pJ_fullvoltage	LEAP 5000-XR	Balmat	08460	Full Voltage	3.48	all hits	0.044277	-16	1
Balmat_XR_8460_40pJ_fullvoltage	LEAP 5000-XR	Balmat	08460	Full Voltage		single hits	0.043839	-26	11
Ruttan_XR_8458_40pJ_fullvoltage	LEAP 5000-XR	Ruttan	08458	Full Voltage	3.47	all hits	0.044243	-17	22
Ruttan_XR_8458_40pJ_fullvoltage	LEAP 5000-XR	Ruttan	08458	Full Voltage		single hits	0.043376	-36	25

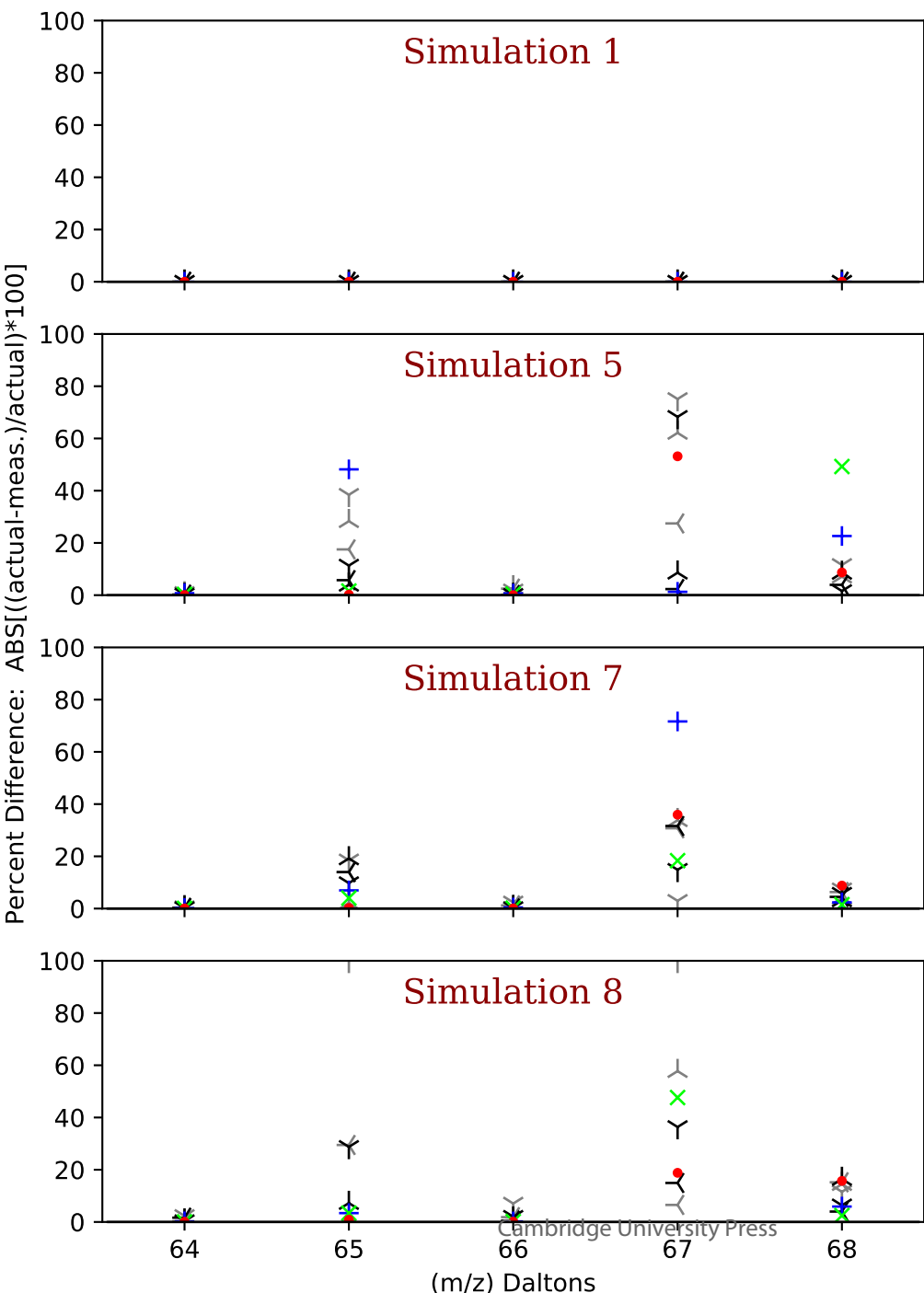
80 pJ, Constant Ion Ratio, $^{32}\text{S}^{1+}/^{32}\text{S}_2^{1+} = 1:1$	Instrument	Standard	Dataset	Voltage Range	Fe <sup>++</sup> /Fe <sup>+</sup>	Data type	$^{34}\text{S}/^{32}\text{S}$	$\delta^{34}\text{S}$ (model CDT)	$\delta^{34}\text{S}$ (Ruttan)
Balmat_XR_9023_fullvoltage	LEAP 5000-XR	Balmat	09023	Full Voltage	3.46	all hits	0.044460	-12	25
Balmat_XR_9023_fullvoltage	LEAP 5000-XR	Balmat	09023	Full Voltage		single hits	0.044103	-20	29
Ruttan_XR_9021_fullvoltage	LEAP 5000-XR	Ruttan	09021	Full Voltage	3.62	all hits	0.043412	-35	-8
Ruttan_XR_9021_fullvoltage	LEAP 5000-XR	Ruttan	09021	Full Voltage		single hits	0.042895	-47	-12

## Unable to Convert Image

The dimensions of this image (in pixels) are too large to be converted. For this image to convert, the total number of pixels (height x width) must be less than 40,000,000 (40 megapixels).

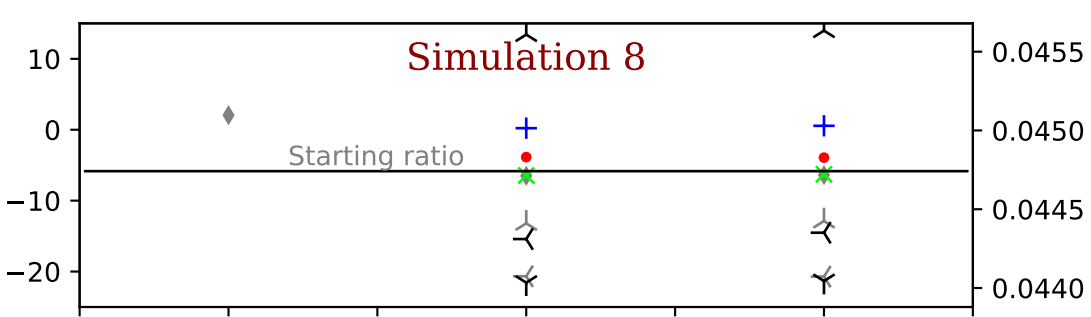
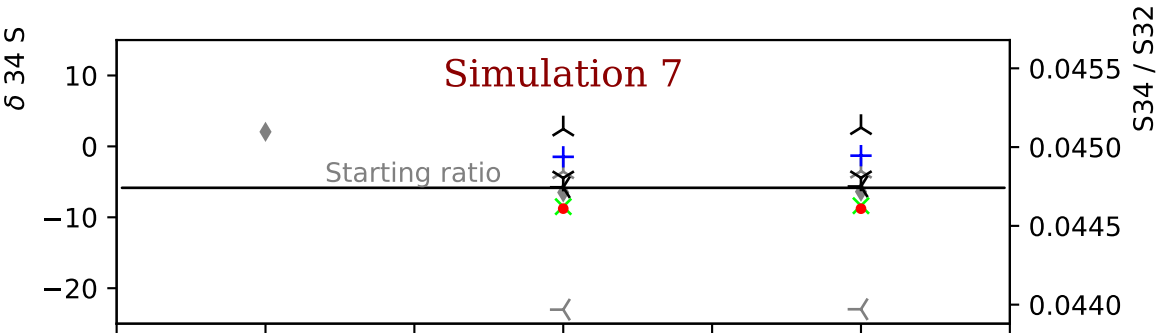
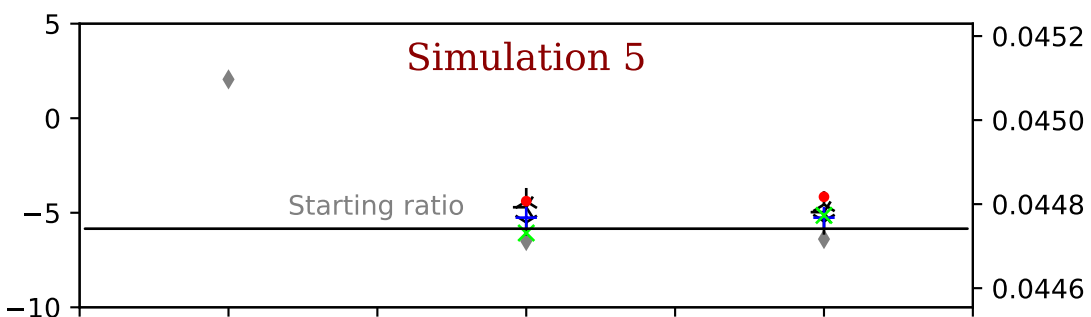
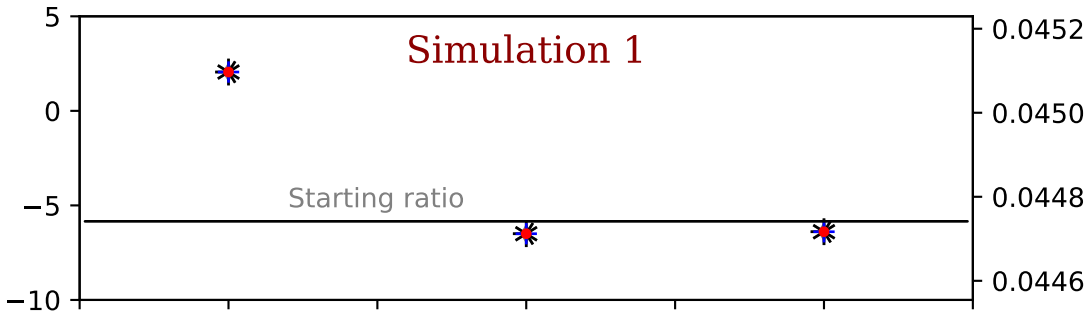
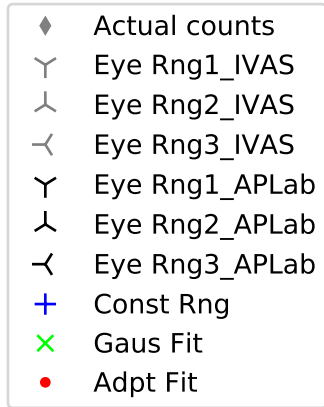
Figure 1: Mass spectrum of dataset R5083\_08493, showing the complexity of the mass spectrum as well as the overlaps present on the main S peak family (34 Da, 33 Da, 34 Da, 36 Da). Note only the main peaks are labeled for sake of clarity.

# Actual vs Measured Counts (% Diff.)



- Eye Rng1\_IVAS
- Eye Rng2\_IVAS
- Eye Rng3\_IVAS
- Eye Rng1\_APLab
- Eye Rng2\_APLab
- Eye Rng3\_APLab
- Const Rng
- Gaus Fit
- Adapt Fit

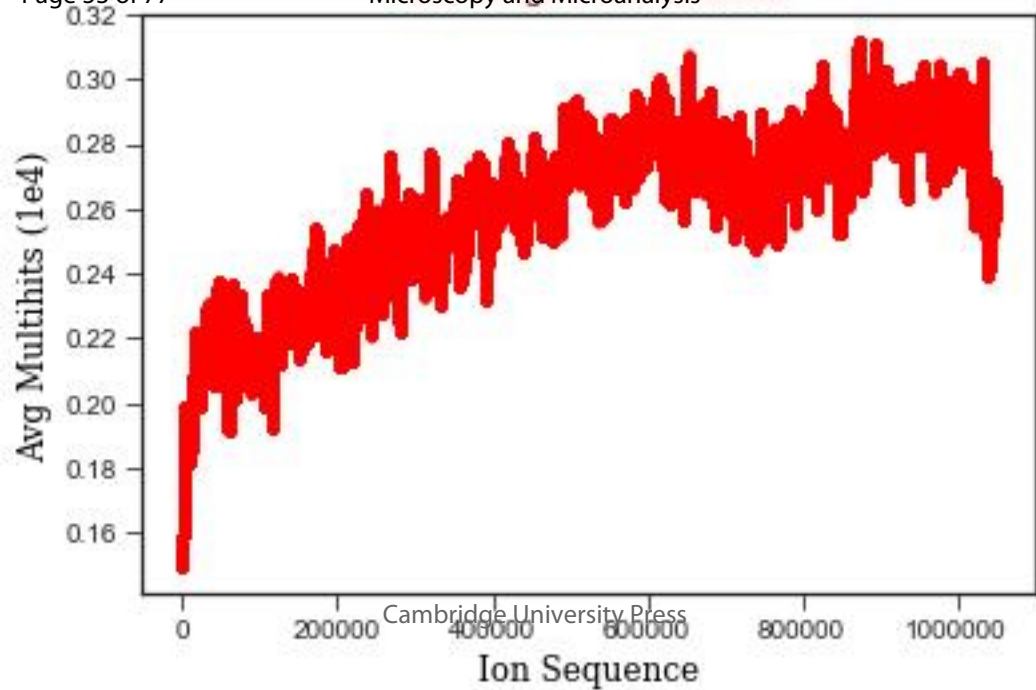




Calculation Method

Cambridge University Press

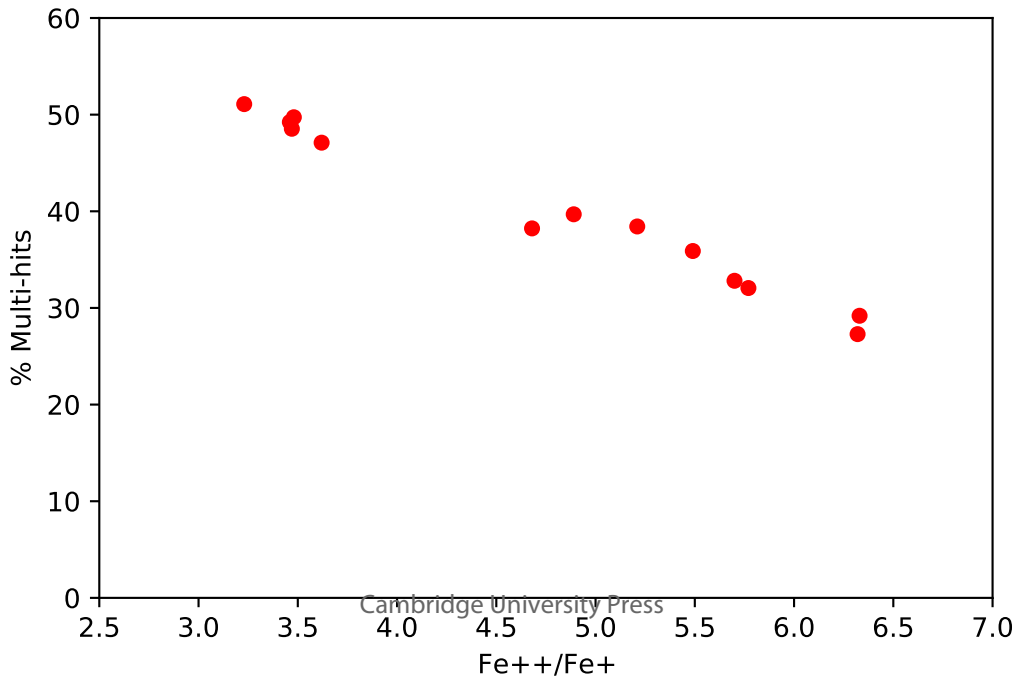
Calculation Method



# Field vs % Multihits

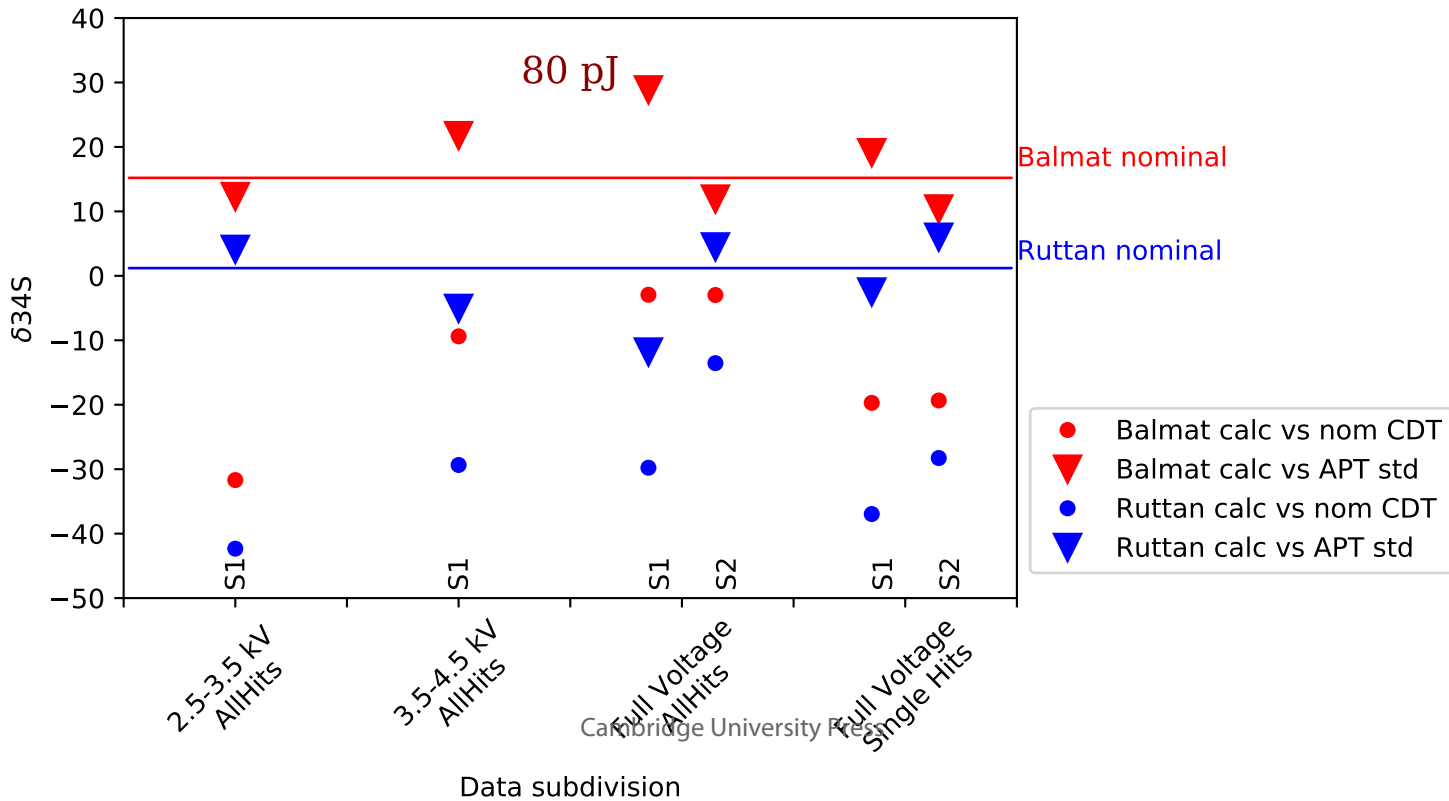
Microscopy and Microanalysis

Page 54 of 77



# Pyrite Standards 634S

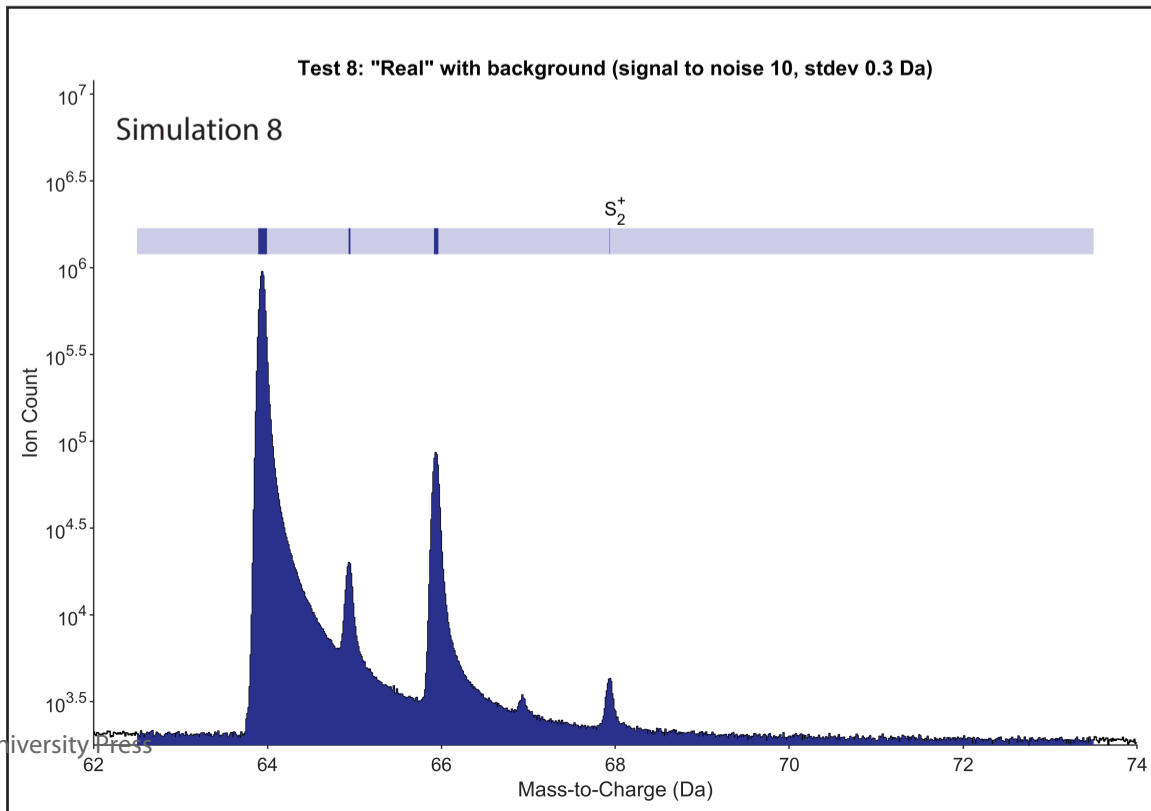
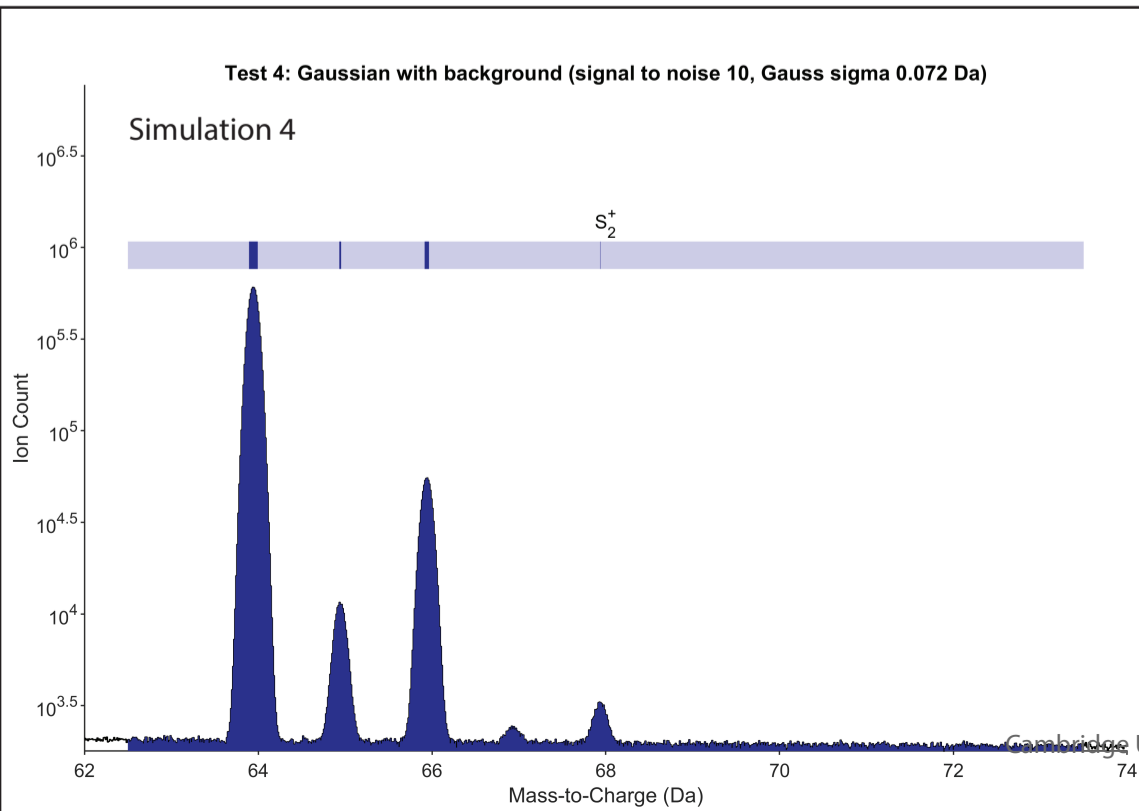
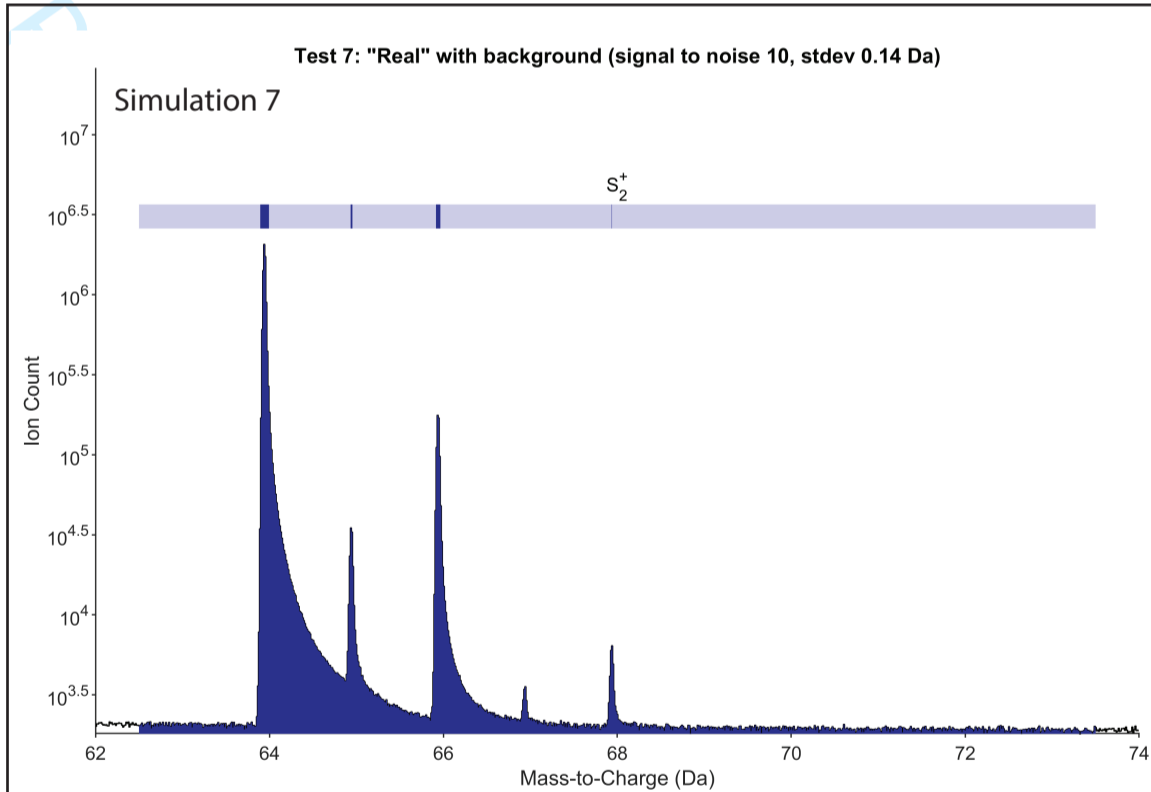
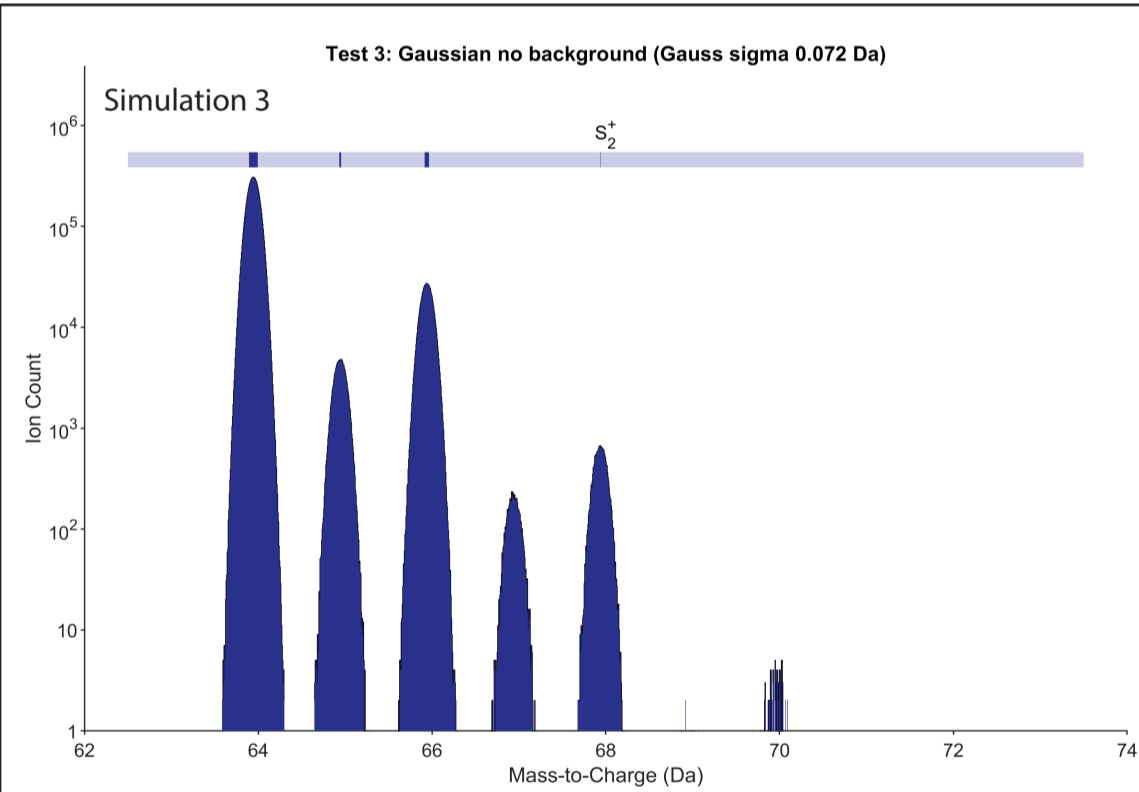
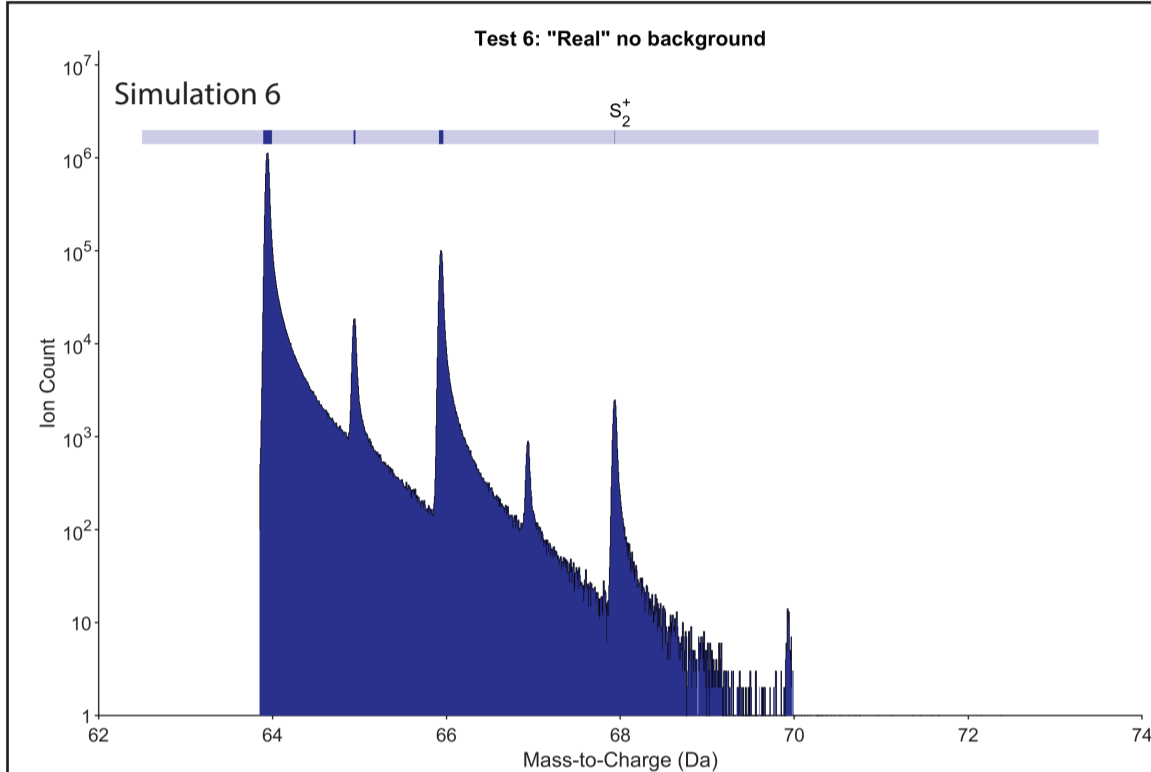
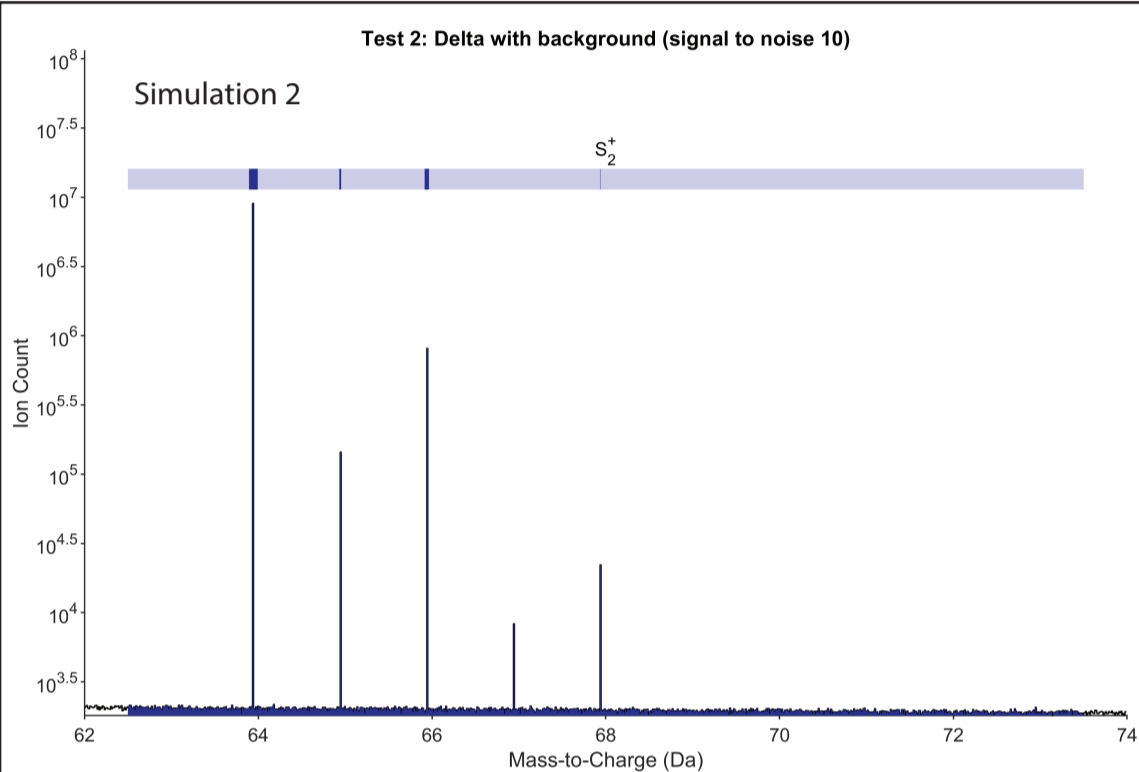
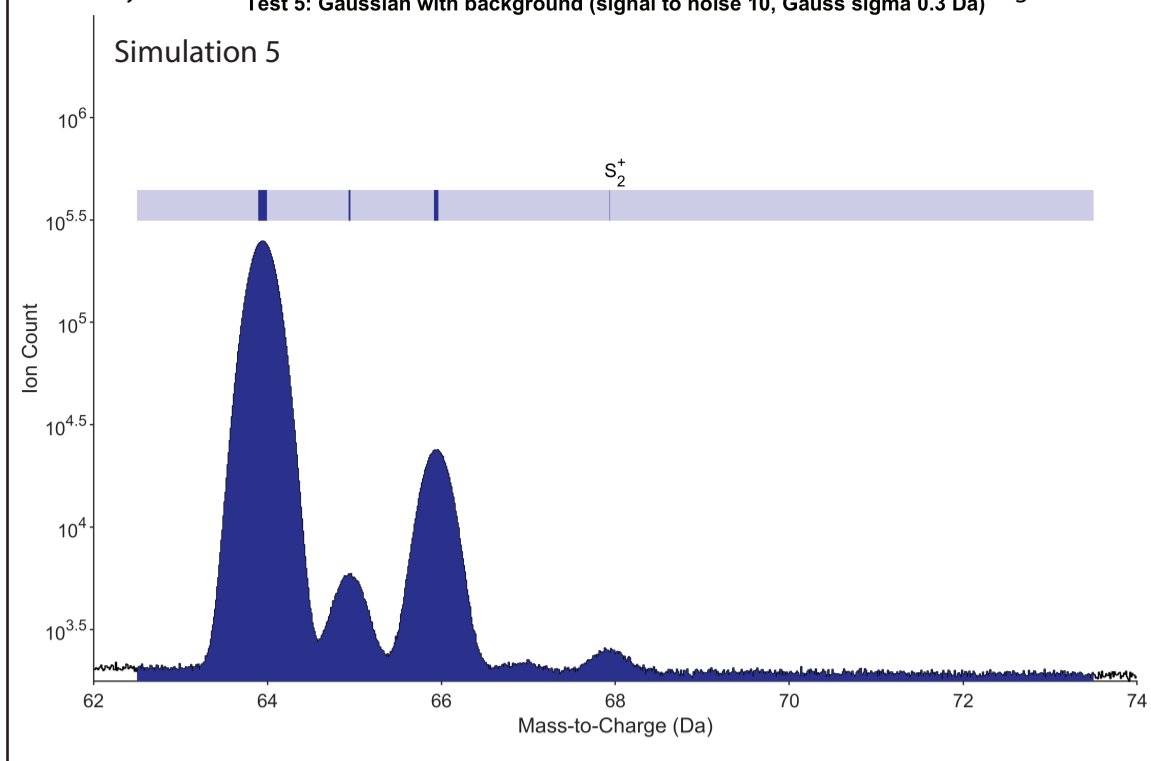
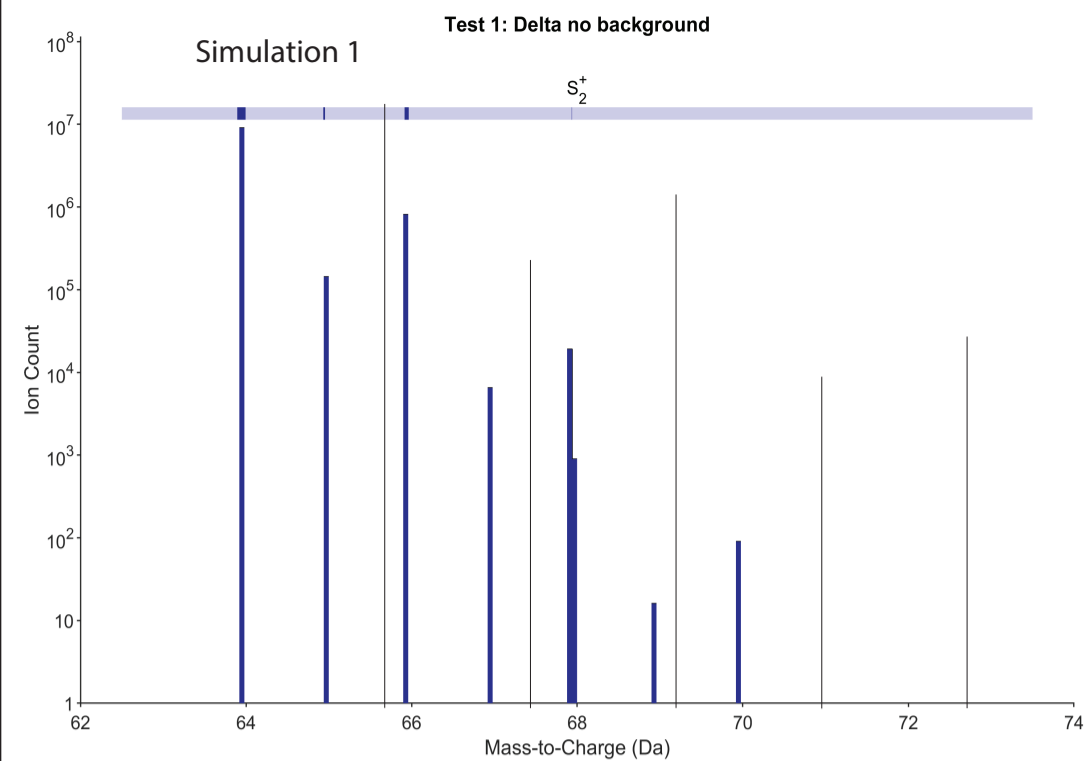
Microscopy and Microanalysis



Analyst #	Sim. #	64 Da		65 Da		66 Da		67
		Start	End	Start	End	Start	End	Start
User 1	1	63.8440	64.1440	64.8440	65.1440	65.8400	66.1400	66.8390
User 2	1	63.5510	64.3330	64.5520	65.3340	65.5500	66.3320	66.5440
User 3	1	63.9160	63.9730	64.9250	64.9610	65.9130	65.9680	66.9180
User 1	2	63.9350	63.9540	64.9390	64.9520	65.9270	65.9510	66.9240
User 2	2	63.5510	64.3330	64.5520	65.3340	65.5500	66.3320	66.5440
User 3	2	63.9200	63.9730	64.9250	64.9610	65.9130	65.9680	66.9180
User 1	3	63.5580	64.3470	64.6080	65.3100	65.5780	66.3360	66.6460
User 2	3	63.5510	64.3330	64.5520	65.3340	65.5500	66.3320	66.5440
User 3	3	63.4920	64.3640	64.5570	65.3430	65.5450	66.3820	66.5980
User 1	4	63.6090	64.2890	64.7040	65.2060	65.6590	66.2450	66.7030
User 2	4	63.5650	64.3040	64.5890	65.2550	65.5210	66.2670	66.6140
User 3	4	63.4740	64.3500	64.6350	65.2820	65.5870	66.3160	66.7130
User 1	5	63.1760	64.5910	64.6270	65.3560	65.4010	66.5960	66.7500
User 2	5	63.2990	64.5500	64.5500	65.3440	65.3540	66.5050	66.6840
User 3	5	63.0550	64.5830	64.5990	65.3420	65.3690	66.5410	66.6040
User 1	6	63.8550	64.8050	64.8790	65.8200	65.8640	66.8260	66.8930
User 2	6	63.6590	64.2340	64.6570	65.2320	65.7720	66.3470	66.6540
User 3	6	63.7920	64.8140	64.8430	65.7600	65.7890	66.8020	66.8380
User 1	7	63.8670	64.8500	64.8880	65.6280	65.8680	66.8610	66.8850
User 2	7	63.6590	64.2340	64.6570	65.2320	65.6610	66.2360	66.6540
User 3	7	63.7790	64.8130	64.8550	65.7790	65.8380	66.6850	66.8380
User 1	8	63.7520	64.8380	64.8570	65.7930	65.8230	66.8010	66.8270
User 2	8	63.6590	64.2340	64.6570	65.2320	65.6610	66.2360	66.6540
User 3	8	63.6770	64.7850	64.7930	65.6400	65.7350	66.6850	66.8200

Da	68 Da	
End	Start	End
67.1390	67.8360	68.1360
67.3260	67.5450	68.3270
66.9610	67.9300	67.9470
66.9520	67.9300	67.9530
67.3260	67.5450	68.3270
66.9610	67.9300	67.9470
67.2310	67.6030	68.2910
67.3260	67.5450	68.3270
67.3450	67.5740	68.3600
67.1460	67.7360	68.1690
67.2420	67.5670	68.2930
67.1660	67.6610	68.2130
67.1510	67.5210	68.2850
67.2790	67.5560	68.2820
67.3400	67.3980	68.4480
67.7270	67.8360	68.7380
67.2290	67.6570	68.2320
67.7020	67.8290	68.5790
67.0550	67.8760	68.0860
67.2290	67.6570	68.2320
67.0750	67.8630	68.1090
67.2140	67.7850	68.2900
67.2290	67.6570	68.2320
67.0580	67.7830	68.1340

For Peer Review



## normalized to 1

			<u>64 counts</u>	<u>65 counts</u>	<u>66 counts</u>	<u>67 counts</u>
<b>Simulation</b>	<b>Peak cnt method</b>	<b>Bkg method</b>				
Sim 1	<i>Actual</i>	<i>none needed</i>	0.902318	0.014295	0.080746	0.000649
		1 <i>IVAS</i>	0.902318	0.014295	0.080746	0.000649
		1 <i>APT Lab</i>	0.902318	0.014295	0.080746	0.000649
	<i>Eye Rangin</i>	2 <i>IVAS</i>	0.902318	0.014295	0.080746	0.000649
		2 <i>APT Lab</i>	0.902318	0.014295	0.080746	0.000649
		3 <i>IVAS</i>	0.902318	0.014295	0.080746	0.000649
		3 <i>APT Lab</i>	0.902318	0.014295	0.080746	0.000649
	<i>Constant Range</i>	<i>IVAS</i>	0.902318	0.014295	0.080746	0.000649
	<i>Gaussian Fit (FWHM) linear</i>					
	<i>Adapt. pk fit</i>	<i>constant</i>	0.902318	0.014295	0.080746	0.000649
Sim 2	<i>Actual</i>	<i>none needed</i>	0.902422	0.014211	0.080738	0.000625
		1 <i>IVAS</i>	0.902408	0.014210	0.080731	0.000639
		1 <i>APT Lab</i>	0.902404	0.014213	0.080739	0.000635
	<i>Eye Rangin</i>	2 <i>IVAS</i>	0.902524	0.014143	0.080741	0.000591
		2 <i>APT Lab</i>	0.902448	0.014175	0.080744	0.000627
		3 <i>IVAS</i>	0.902400	0.014221	0.080727	0.000638
		3 <i>APT Lab</i>	0.902410	0.014218	0.080727	0.000634
	<i>Constant Range</i>	<i>APT Lab</i>	0.902482	0.014191	0.080716	0.000631
	<i>Gaussian Fit (FWHM) linear</i>					
	<i>Adapt. pk fit</i>	<i>constant</i>	0.902421	0.014209	0.080738	0.000625
Sim 3	<i>Actual</i>	<i>none needed</i>	0.902088	0.014277	0.080980	0.000647
		1 <i>IVAS</i>	0.902088	0.014277	0.080980	0.000647
		1 <i>APT Lab</i>	0.902088	0.014277	0.080980	0.000647
	<i>Eye Rangin</i>	2 <i>IVAS</i>	0.902088	0.014277	0.080980	0.000647
		2 <i>APT Lab</i>	0.902088	0.014277	0.080980	0.000647
		3 <i>IVAS</i>	0.902088	0.014277	0.080980	0.000647
		3 <i>APT Lab</i>	0.902088	0.014277	0.080980	0.000647
	<i>Constant Range</i>	<i>APT Lab</i>	0.902117	0.014279	0.080987	0.000630
	<i>Gaussian Fit (FWHM) linear</i>		0.902025	0.014170	0.081122	0.000713
	<i>Adapt. pk fit</i>	<i>constant</i>	0.902080	0.014267	0.080996	0.000644
Sim 4	<i>Actual</i>	<i>none needed</i>	0.902446	0.014211	0.080714	0.000638
		1 <i>IVAS</i>	0.902193	0.014116	0.080870	0.000884
		1 <i>APT Lab</i>	0.902445	0.014228	0.080727	0.000633
	<i>Eye Rangin</i>	2 <i>IVAS</i>	0.902178	0.014191	0.080601	0.000611
		2 <i>APT Lab</i>	0.902463	0.014226	0.080724	0.000624
		3 <i>IVAS</i>	0.901436	0.015010	0.080618	0.000841
		3 <i>APT Lab</i>	0.902450	0.014245	0.080702	0.000629
	<i>Constant Range</i>	<i>APT Lab</i>	0.902525	0.014235	0.080667	0.000638
	<i>Gaussian Fit (FWHM) linear</i>		0.901900	0.014230	0.080648	0.001088
	<i>Adapt. pk fit</i>	<i>constant</i>	0.902462	0.014203	0.080639	0.000686
Sim 5	<i>Actual</i>	<i>none needed</i>	0.902240644	0.014245654	0.080887974	0.000637407
		1 <i>IVAS</i>	0.909896005	0.008771452	0.079415592	0.000158689
		1 <i>APT Lab</i>	0.904223641	0.012632921	0.080984269	0.000202283



	<b>Eye Rangin</b>	<b>2 IVAS</b>	0.896352719	0.018280659	0.083277856	0.000241392	
		<b>2 APT Lab</b>	0.902947924	0.013682173	0.080968127	0.000582662	
		<b>3 IVAS</b>	0.899317377	0.011749941	0.082903092	0.000462345	
		<b>3 APT Lab</b>	0.902915142	0.013427944	0.080937738	0.000652279	
	<b>Constant Range</b>	<b>APT Lab</b>	0.909017022	0.007383716	0.08141581	0.000645522	
	<b>Gaussian Fit (FWHM)</b>	<b>linear</b>	0.899611134	0.014019648	0.080536226	0.00286533	
	<b>Adapt. pk fit</b>	<b>constant</b>	0.90177589	0.014218601	0.080868008	0.0009763	
	<b>Sim 6</b>	<b>Actual</b>	<b>none need</b>	0.902257542	0.01432024	0.080775192	0.000630706
<b>1 IVAS</b>			0.904698878	0.013849068	0.07958078	0	
<b>1 APT Lab</b>			0.902115099	0.014794896	0.080616698	0.000509313	
<b>Eye Rangin</b>		<b>2 IVAS</b>	0.90183008	0.013778033	0.081791287	0.00060253	
		<b>2 APT Lab</b>	0.900050043	0.015481984	0.081631215	0.000824572	
		<b>3 IVAS</b>	0.904428247	0.011759052	0.081079572	0.000832052	
		<b>3 APT Lab</b>	0.901691875	0.01479123	0.080797228	0.000756773	
		<b>Constant Range</b>	<b>APT Lab</b>	0.901936679	0.01456112	0.080786913	0.000696181
		<b>Gaussian Fit (FWHM)</b>	<b>linear</b>	0.902346545	0.01417704	0.080817475	0.000631945
<b>Adapt. pk fit</b>		<b>constant</b>	0.9023554	0.0142861	0.0808003	0.0005821	
<b>Sim 7</b>		<b>Actual</b>	<b>none need</b>	0.902459947	0.014240854	0.080672871	0.000633507
			<b>1 IVAS</b>	0.907144186	0.011611837	0.078783121	0.000614797
	<b>1 APT Lab</b>		0.901136939	0.015627867	0.080816169	0.000539522	
	<b>Eye Rangin</b>	<b>2 IVAS</b>	0.901757425	0.014547371	0.080935854	0.000847723	
		<b>2 APT Lab</b>	0.898424369	0.016973062	0.081144263	0.001402908	
		<b>3 IVAS</b>	0.905754204	0.012249865	0.079690481	0.000438719	
		<b>3 APT Lab</b>	0.900746834	0.016228182	0.080688158	0.000433215	
		<b>Constant Range</b>	<b>APT Lab</b>	0.900630342	0.015232457	0.081009779	0.00108739
		<b>Gaussian Fit (FWHM)</b>	<b>linear</b>	0.901865823	0.014814727	0.080546895	0.000749661
	<b>Adapt. pk fit</b>	<b>constant</b>	0.9029538	0.0142065	0.0806164	0.0004058	
	<b>Sim 8</b>	<b>Actual</b>	<b>none need</b>	0.902230583	0.014207948	0.080908341	0.000649907
			<b>1 IVAS</b>	0.9230227	0	0.075205287	0
<b>1 APT Lab</b>			0.899390327	0.018292039	0.079300768	0.000886182	
<b>Eye Rangin</b>		<b>2 IVAS</b>	0.902490243	0.013976857	0.08021399	0.001025285	
		<b>2 APT Lab</b>	0.897536586	0.015236924	0.081934901	0.002959021	
		<b>3 IVAS</b>	0.899880424	0.018395772	0.07941766	0.000607485	
		<b>3 APT Lab</b>	0.917042553	-0.00120158	0.081328999	0.000747022	
		<b>Constant Range</b>	<b>APT Lab</b>	0.899971558	0.014689764	0.081083317	0.00213386
		<b>Gaussian Fit (FWHM)</b>	<b>linear</b>	0.902500133	0.013726744	0.080761235	0.000959539
<b>Adapt. pk fit</b>		<b>constant</b>	0.902706	0.014085	0.0809931	0.0005276	

<u>68 counts</u>	<u>d34S</u> <u>Monte Carlo</u>	<u>d34S</u> <u>Multinomial</u>	<u>d34S</u> <u>Linear Lst. Sqr.</u>	<u>d34S</u> <u>Actual</u>
0.001993	2.05	-6.50	-6.39	-5.84
0.001993	2.05	-6.50	-6.39	-5.84
0.001993	2.05	-6.50	-6.39	-5.84
0.001993	2.05	-6.50	-6.39	-5.84
0.001993	2.05	-6.50	-6.39	-5.84
0.001993	2.05	-6.50	-6.39	-5.84
0.001993	2.05	-6.50	-6.39	-5.84
0.001993	2.05	-6.50	-6.39	-5.84
0.001992	2.05	-6.50	-6.39	-5.84
0.002005	-15.39	-6.69	-6.58	-5.84
0.002012	-4.75	-6.77	-6.65	-5.84
0.002009	-8.50	-6.67	-6.55	-5.84
0.002001	-38.27	-6.76	-6.66	-5.84
0.002006	-10.86	-6.65	-6.54	-5.84
0.002014	-4.75	-6.81	-6.70	-5.84
0.002011	-7.77	-6.82	-6.71	-5.84
0.001980	-9.39	-7.03	-6.93	-5.84
0.002007	-15.42	-6.70	-6.58	-5.84
0.002007	0.58	-3.25	-3.25	-5.84
0.002007	0.58	-3.36	-3.25	-5.84
0.002007	0.58	-3.36	-3.25	-5.84
0.002007	0.58	-3.36	-3.25	-5.84
0.002007	0.58	-3.36	-3.25	-5.84
0.002007	0.58	-3.36	-3.25	-5.84
0.002007	0.58	-3.36	-3.25	-5.84
0.001987	-11.55	-3.20	-3.20	-5.84
0.001970	49.80	-1.53	-1.44	-5.84
0.002012	-0.93	-3.14	-3.04	-5.84
0.001991	-4.80	-6.92	-6.92	-5.84
0.001937	65.06	-4.81	-4.72	-5.84
0.001968	-9.24	-6.86	-6.77	-5.84
0.002420	-27.15	-8.12	-7.77	-5.84
0.001964	-16.81	-6.92	-6.83	-5.84
0.002096	100.59	-7.18	-6.99	-5.84
0.001974	-11.55	-7.18	-7.09	-5.84
0.001934	-6.28	-7.61	-7.61	-5.84
0.002134	142.42	-7.24	-7.01	-5.84
0.002010	31.55	-7.97	-7.84	-5.84
0.001988321	-6.99	-4.56	-4.56	-5.84
0.001758262	-374.50	-30.58	-30.58	-5.84
0.001956886	-405.15	-5.51	-5.45	-5.84

0.001847374	-450.54	31.05	30.93	-5.84
0.001819114	-30.12	-4.39	-4.56	-5.84
0.005567246	-54.31	23.70	25.94	-5.84
0.002066897	35.44	-4.71	-4.97	-5.84
0.00153793	-35.42	-5.26	-5.26	-5.84
0.002967663	498.87	-6.07	-5.14	-5.84
0.0021612	138.28	-4.39	-4.16	-5.84
0.00201632	-11.55	-6.07	-5.95	-5.84
0.001871275	6026.58	-23.37	-23.36	-5.84
0.001963994	-129.77	-7.91	-7.83	-5.84
0.001998069	-10.08	6.97	7.05	-5.84
0.002012186	70.05	6.81	6.92	-5.84
0.001901077	64.29	-4.49	-4.42	-5.84
0.001962893	52.22	-5.22	-5.13	-5.84
0.002019107	27.64	-5.60	-5.47	-5.84
0.002026995	-7.00	-5.63	-5.51	-5.84
0.0019761	-49.19	-5.86	-5.78	-5.84
0.001992822	-9.24	-7.54	-7.44	-5.84
0.001846058	25.22	-35.58	-35.50	-5.84
0.001879502	-125.67	-4.46	-4.44	-5.84
0.001911627	51.43	-3.56	-3.49	-5.84
0.002055397	128.74	2.45	2.65	-5.84
0.001866731	-117.74	-23.02	-22.97	-5.84
0.001903611	-250.04	-5.77	-5.65	-5.84
0.002040033	109.90	-1.47	-1.31	-5.84
0.002022894	56.23	-8.50	-8.37	-5.84
0.0018175	-206.51	-8.78	-8.79	-5.84
0.002003221	5.92	-4.39	-4.28	-5.84
0.001772013	6026.58	-94.79	-94.67	-5.84
0.002130684	26.93	-21.56	-21.34	-5.84
0.002293624	186.90	-13.20	-12.88	-5.84
0.002332568	305.70	13.42	13.97	-5.84
0.00169866	-153.34	-20.66	-20.71	-5.84
0.002083005	52.35	-15.42	-14.52	-5.84
0.002121501	207.92	0.22	0.56	-5.84
0.002052348	109.90	-6.45	-6.28	-5.84
0.0016883	-91.25	-3.86	-3.94	-5.84

**Canyon diablo Triolite**

<b>Ruttan Pyrite</b>		
<b>Balmat Pyrite</b>		

<b>80 pJ, Varying Ion Ratio</b>	<b>Ions e6</b>	<b>Instrument</b>
Balmat_XR_8493_80pJ_2500-3500V_allHits	61	LEAP 5000-XR
Balmat_XR_8493_80pJ_3500_4500V_allHits	61	LEAP 5000-XR
Balmat_XR_8493_80pJ_fullvoltage_allHits	61	LEAP 5000-XR
Balmat_XR_8493_80pJ_fullvoltage_singleHits		LEAP 5000-XR
Balmat_XR_11434_80pJ_fullvoltage_allHits		LEAP 5000-XR
Balmat_XR_11434_80pJ_fullvoltage_singleHits		LEAP 5000-XR
Ruttan_XR_8492_80pJ_2500-3500V_allHits	25	LEAP 5000-XR
Ruttan_XR_8492_80pJ_3500-4500V_allHits	25	LEAP 5000-XR
Ruttan_XR_8492_80pJ_fullvoltage_allHits	25	LEAP 5000-XR
Ruttan_XR_8492_80pJ_fullvoltage_singleHits		LEAP 5000-XR
Ruttan_XR_11435_80pJ_fullvoltage_allHits		LEAP 5000-XR
Ruttan_XR_11435_80pJ_fullvoltage_singleHits		LEAP 5000-XR
<b>40 pJ, Varying Ion Ratio</b>		
Balmat_XR_8462_40pJ_full_voltage_allHits	33	LEAP 5000-XR
Balmat_XR_8462_40pJ_fullvoltage_singleHits		LEAP 5000-XR
Balmat_XR_8460_40pJ_fullvoltage_allHits	20	LEAP 5000-XR
Balmat_XR_8460_40pJ_fullvoltage_singleHits		LEAP 5000-XR
Ruttan_XR_8458_40pJ_fullvoltage_allHits	16	LEAP 5000-XR
Ruttan_XR_8458_40pJ_fullvoltage_singleHits		LEAP 5000-XR
<b>80 pJ, Constant Ion Ratio, <math>^{32}\text{S}^{1+}/^{32,32}\text{S}_2^{1+} = 1:1</math></b>		
Balmat_XR_9023_fullvoltage_allHits	26	LEAP 5000-XR
Balmat_XR_9023_fullvoltage_singleHits		LEAP 5000-XR
Ruttan_XR_9021_fullvoltage_allHits	20	LEAP 5000-XR

Ruttan\_XR\_9021\_fullvoltage\_singleHits

LEAP 5000-XR

**\*\*\*\* NOTE \*\*\*\* "Full voltage range" is not really using**

**\*\*\*\* NOTE \*\*\*\* Some calculations are done in-table, if**

For Peer Review

			<b>Standard</b>	<b>Mineral</b>
			<b>Canyon Diablo</b>	<b>Troilite</b>
			<b>Ruttan</b>	<b>Pyrite</b>
			<b>Balmat</b>	<b>Pyrite</b>

<b>Standard</b>	<b>Cond.</b>	<b>Dataset</b>	<b>Voltage Range</b>	<b>Fe<sup>++</sup>/Fe<sup>+</sup></b>
Balmat	80pJ	08493	2500-3500V	6.33
Balmat	80pJ	08493	3500-4500V	5.49
Balmat	80pJ	08493	Full voltage	5.21
Balmat	80pJ	08493	Full voltage	
Balmat	80pJ	11434	Full voltage	4.89
Balmat	80pJ	11434	Full voltage	
Ruttan	80pJ	08492	2500-3500V	6.32
Ruttan	80pJ	08492	3500-4500V	5.7
Ruttan	80pJ	08492	Full Voltage	5.77
Ruttan	80pJ	08492	Full Voltage	
Ruttan	80pJ	11435	Full Voltage	4.68
Ruttan	80pJ	11435	Full Voltage	

Balmat	40pJ	08462	Full Voltage	3.23
Balmat	40pJ	08462	Full Voltage	
Balmat	40pJ	08460	Full Voltage	3.48
Balmat	40pJ	08460	Full Voltage	
Ruttan	40pJ	08458	Full Voltage	3.47
Ruttan	40pJ	08458	Full Voltage	

Balmat	S <sup>+</sup> /S <sub>2</sub> <sup>+</sup> =1:1	09023	Full Voltage	3.46
Balmat	S <sup>+</sup> /S <sub>2</sub> <sup>+</sup> =1:1	09023	Full Voltage	
Ruttan	S <sup>+</sup> /S <sub>2</sub> <sup>+</sup> =1:1	09021	Full Voltage	3.62

Ruttan

S+/S2+=1:1

09021

Full Voltage

the full voltage range.

copying to another table, be sure to use "paste v

For Peer Review

	<b>Formula</b>	<b><math>^{34}\text{S}/^{32}\text{S}</math></b>	<b><math>\delta^{34}\text{S}</math> (CDT)</b>
	<b>FeS</b>	<b>0.045005</b>	<b>0</b>
	<b>FeS2</b>	<b>0.045059</b>	<b>1.2</b>
	<b>FeS2</b>	<b>0.045684</b>	<b>15.1</b>
<b>% Multihits</b>	<b>Data type</b>	<b><math>^{34}\text{S}/^{32}\text{S}</math></b>	<b><math>\delta^{34}\text{S}</math> (model CDT)</b>
29.19	all hits	0.043578	-32
35.89	all hits	0.044582	-9
38.43	all hits	0.044872	-3
	single hits	0.044118	-20
39.69	all hits	0.044871	-3
	single hits	0.044134	-19
27.29	all hits	0.043099	-42
32.81	all hits	0.043684	-29
32.06	all hits	0.043665	-30
	single hits	0.043341	-37
38.23	all hits	0.044395	-14
	single hits	0.043732	-28
51.09	all hits	0.045822	18
	single hits	0.044802	-5
49.73	all hits	0.045561	12
	single hits	0.044549	-10
48.54	all hits	0.045188	4
	single hits	0.044121	-20
49.23	all hits	0.045829	18
	single hits	0.044806	-4
47.1	all hits	0.044894	-2



	single hits	0.043822	-26
--	-------------	----------	-----



alues"

For Peer Review

<b><math>\delta^{34}\text{S}</math> (APT Stand)</b>	
12	
22	
29	
19	
12	
10	
4	
-5	
-12	
-2	
4	
6	
15	
17	
9	
11	
1	
0	
22	
24	
-5	

Review

-7



For Peer Review

**Canyon diablo Triolite****Ruttan Pyrite****Balmat Pyrite**

<b>80 pJ, Varying Ion Ratio</b>	<b>Instrument</b>	<b>Standard</b>
Balmat_XR_8493_80pJ_fullvoltage	LEAP 5000-XR	Balmat
Balmat_XR_11434_80pJ_fullvoltage	LEAP 5000-XR	Balmat
Ruttan_XR_8492_80pJ_fullvoltage	LEAP 5000-XR	Ruttan
Ruttan_XR_11435_80pJ_fullvoltage	LEAP 5000-XR	Ruttan
<b>40 pJ, Varying Ion Ratio</b>		
Balmat_XR_8462_40pJ_full voltage	LEAP 5000-XR	Balmat
Balmat_XR_8460_40pJ_fullvoltage	LEAP 5000-XR	Balmat
Ruttan_XR_8458_40pJ_fullvoltage	LEAP 5000-XR	Ruttan
<b>80 pJ, Constant Ion Ratio, <math>^{32}\text{S}^{1+}/^{32,32}\text{S}_2^{1+} = 1:1</math></b>		
Balmat_XR_9023_fullvoltage	LEAP 5000-XR	Balmat
Ruttan_XR_9021_fullvoltage	LEAP 5000-XR	Ruttan

	<b>Standard</b>	<b>Mineral</b>	<b>Formula</b>
	<b>Canyon Diablo</b>	<b>Troilite</b>	<b>FeS</b>
	<b>Ruttan</b>	<b>Pyrite</b>	<b>FeS<sub>2</sub></b>
	<b>Balmat</b>	<b>Pyrite</b>	<b>FeS<sub>2</sub></b>

<b>Dataset</b>	<b>Voltage Range</b>	<b>Fe<sup>++</sup>/Fe<sup>+</sup></b>	<b>Data type</b>
08493	Full voltage	5.21	all hits
11434	Full voltage		all hits
08492	Full Voltage	5.77	all hits
11435	Full Voltage		all hits

08462	Full Voltage	3.23	all hits
08460	Full Voltage	3.48	all hits
08458	Full Voltage	3.47	all hits

09023	Full Voltage	3.46	all hits
09021	Full Voltage	3.62	all hits

$^{34}\text{S}/^{32}\text{S}$	$\delta^{34}\text{S}$ (CDT)	
<b>0.045005</b>	<b>0</b>	
<b>0.045059</b>	<b>1.2</b>	
<b>0.045684</b>	<b>15.1</b>	

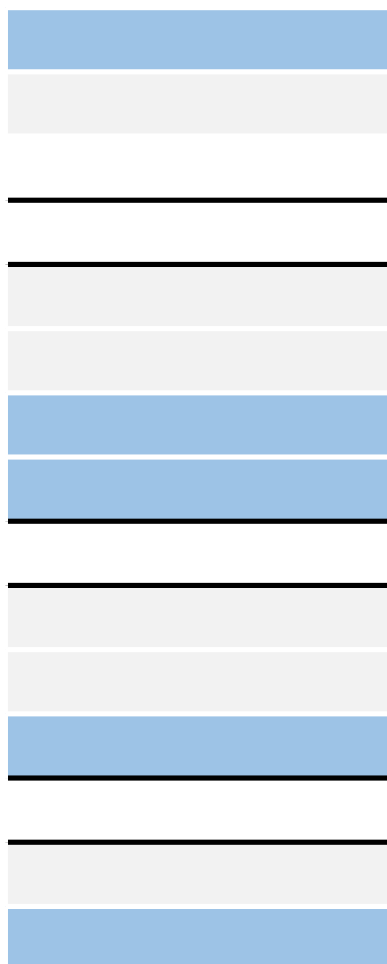
$^{34}\text{S}/^{32}\text{S}$	$\delta^{34}\text{S}$ (model CDT)	$\delta^{34}\text{S}$ (Ruttan)
0.045565	12	29
0.045591	13	14
0.044334	-15	-12
0.045015	0	2

0.046207	27	12
0.046123	25	10
0.045699	15	4

0.046126	25	19
0.045317	7	-2



For Peer Review

### Canyon diablo Triolite

Ruttan Pyrite

Balmat Pyrite

<b>80 pJ, Varying Ion Ratio</b>	<b>Instrument</b>	<b>Standard</b>
Balmat_XR_8493_80pJ_fullvoltage	LEAP 5000-XR	Balmat
Balmat_XR_8493_80pJ_fullvoltage	LEAP 5000-XR	Balmat
Ruttan_XR_8492_80pJ_fullvoltage	LEAP 5000-XR	Ruttan
Ruttan_XR_8492_80pJ_fullvoltage	LEAP 5000-XR	Ruttan
<b>40 pJ, Varying Ion Ratio</b>		
Balmat_XR_8462_40pJ_full voltage	LEAP 5000-XR	Balmat
Balmat_XR_8462_40pJ_fullvoltage	LEAP 5000-XR	Balmat
Balmat_XR_8460_40pJ_fullvoltage	LEAP 5000-XR	Balmat
Balmat_XR_8460_40pJ_fullvoltage	LEAP 5000-XR	Balmat
Ruttan_XR_8458_40pJ_fullvoltage	LEAP 5000-XR	Ruttan
Ruttan_XR_8458_40pJ_fullvoltage	LEAP 5000-XR	Ruttan
<b>80 pJ, Constant Ion Ratio, <math>^{32}\text{S}^{1+}/^{32,32}\text{S}_2^{1+} = 1:1</math></b>		
Balmat_XR_9023_fullvoltage	LEAP 5000-XR	Balmat
Balmat_XR_9023_fullvoltage	LEAP 5000-XR	Balmat
Ruttan_XR_9021_fullvoltage	LEAP 5000-XR	Ruttan
Ruttan_XR_9021_fullvoltage	LEAP 5000-XR	Ruttan



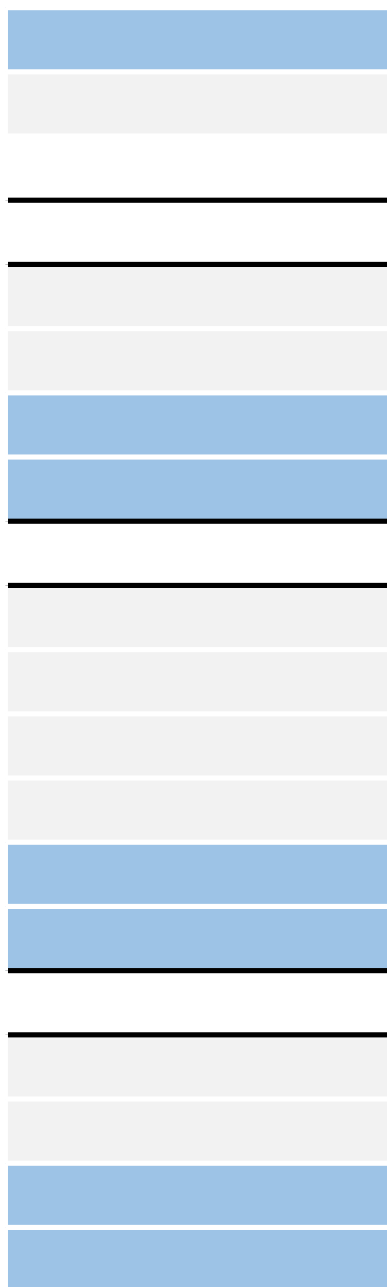
	<b>Standard</b>	<b>Mineral</b>	<b>Formula</b>
	<b>Canyon Diablo</b>	<b>Troilite</b>	<b>FeS</b>
	<b>Ruttan</b>	<b>Pyrite</b>	<b>FeS<sub>2</sub></b>
	<b>Balmat</b>	<b>Pyrite</b>	<b>FeS<sub>2</sub></b>

<b>Dataset</b>	<b>Voltage Range</b>	<b>Fe<sup>++</sup>/Fe<sup>+</sup></b>	<b>Data type</b>
08493	Full voltage	5.21	all hits
08493	Full voltage		single hits
08492	Full Voltage	5.77	all hits
08492	Full Voltage		single hits

08462	Full Voltage	3.23	all hits
08462	Full Voltage		single hits
08460	Full Voltage	3.48	all hits
08460	Full Voltage		single hits
08458	Full Voltage	3.47	all hits
08458	Full Voltage		single hits

09023	Full Voltage	3.46	all hits
09023	Full Voltage		single hits
09021	Full Voltage	3.62	all hits
09021	Full Voltage		single hits

$^{34}\text{S}/^{32}\text{S}$	$\delta^{34}\text{S}$ (CDT)	
<b>0.045005</b>	<b>0</b>	
<b>0.045059</b>	<b>1.2</b>	
<b>0.045684</b>	<b>15.1</b>	
$^{34}\text{S}/^{32}\text{S}$	$\delta^{34}\text{S}$ (model CDT)	$\delta^{34}\text{S}$ (Ruttan)
0.044105	-20	20
0.043620	-31	15
0.043298	-38	-3
0.043009	-44	1
0.044596	-9	8
0.044261	-17	11
0.044277	-16	1
0.043839	-26	11
0.044243	-17	22
0.043376	-36	25
0.044460	-12	25
0.044103	-20	29
0.043412	-35	-8
0.042895	-47	-12



For Peer Review